Plasmoids in relativistic reconnection, from birth to adulthood: first they grow, then they go

Lorenzo Sironi,[1][★] Dimitrios Giannios[2] and Maria Petropoulou[2][†]

[1]*Department of Astronomy, Columbia University, 550 W 120th St, New York, NY 10027, USA*
[2]*Department of Physics and Astronomy, Purdue University, 525 Northwestern Avenue, West Lafayette, IN 47907, USA*

ABSTRACT

Blobs, or quasi-spherical emission regions containing relativistic particles and magnetic fields, are often assumed ad hoc in emission models of relativistic astrophysical jets, yet their physical origin is still not well understood. Here, we employ a suite of large-scale 2D particle-in-cell simulations in electron–positron plasmas to demonstrate that relativistic magnetic reconnection can naturally account for the formation of quasi-spherical plasmoids filled with high-energy particles and magnetic fields. Our simulations extend to unprecedentedly long temporal and spatial scales, so we can capture the asymptotic physics independently of the initial setup. We characterize the properties of the plasmoids, continuously generated as a self-consistent by-product of the reconnection process: they are in rough energy equipartition between particles and magnetic fields; the upper energy cutoff of the plasmoid particle spectrum is proportional to the plasmoid width w, corresponding to a Larmor radius $\sim 0.2\,w$; the plasmoids grow in size at ~ 0.1 of the speed of light, with most of the growth happening while they are still non-relativistic ('first they grow'); their growth is suppressed once they get accelerated to relativistic speeds by the field line tension, up to the Alfvén speed ('then they go'). The largest plasmoids reach a width $w^{\rm max} \sim 0.2\,L$ independently of the system length L, they have nearly isotropic particle distributions and contain the highest energy particles, whose Larmor radius is $\sim 0.03\,L$. The latter can be regarded as the Hillas criterion for relativistic reconnection. We briefly discuss the implications of our results for the high-energy emission from relativistic jets and pulsar winds.

Key words: magnetic reconnection – MHD – radiation mechanisms: non-thermal – gamma-ray burst: general – pulsars: general – galaxies: jets.

1 INTRODUCTION

It is generally thought that pulsar winds and the relativistic jets of blazars and gamma-ray bursts (GRBs) are launched hydromagnetically (Spruit 2010). The strong magnetic fields threading a rotating compact object or the associated accretion disc serve to convert the rotational energy of the central engine into the power of the relativistic outflow. Since the energy is carried initially in the form of Poynting flux, it is a fundamental question how and where the energy in the fields is transferred to the plasma, and then radiated away to power the observed emission. Because of their tightly wound-up magnetic fields, jets may be susceptible to magnetohydrodynamic (MHD) kink instabilities. At their non-linear stages, these MHD instabilities introduce small-scale magnetic field reversals that lead to dissipation of magnetic energy through magnetic reconnection (Begelman 1998; Spruit, Daigne & Drenkhahn 2001). Alternatively, the outflow may contain current sheets from its base, as it is the case in pulsar winds, if the pulsar rotational and magnetic axes are not aligned (Lyubarsky & Kirk 2001). In either case, field dissipation via magnetic reconnection has been often invoked to explain the non-thermal signatures of pulsar wind nebulae (PWNe; e.g. Lyubarsky & Kirk 2001; Kirk & Skjæraasen 2003; Lyubarsky 2003; Pétri & Lyubarsky 2007; Sironi & Spitkovsky 2011b), jets from active galactic nuclei (AGNs; e.g. Romanova & Lovelace 1992; Giannios, Uzdensky & Begelman 2009, 2010; Giannios 2013) and GRBs (e.g. Thompson 1994, 2006; Usov 1994; Spruit et al. 2001; Drenkhahn & Spruit 2002; Lyutikov & Blandford 2003; Giannios 2008). Despite decades of research, we have no reliable theory built from first principles for the particle distribution, geometry and magnetic field to be expected in the radiating regions of a reconnection-dominated system.

In relativistic astrophysical outflows, reconnection proceeds in the 'relativistic' regime in which the magnetic energy per particle can exceed the rest mass energy (or equivalently, the magnetization

σ is larger than unity). The flow dynamics in relativistic reconnection has been satisfactorily described by analytical studies (e.g. Lyutikov & Uzdensky 2003; Lyubarsky 2005), even though analytical models still have to make assumptions on the resistive processes at work, that critically affect the geometry of the layer. However, the acceleration process of the emitting particles can only be captured from first principles by means of fully-kinetic particle-in-cell (PIC) simulations. Energization of particles in relativistic reconnection of pair plasmas has been investigated in a number of PIC studies, both in two dimensions (2D; e.g. Zenitani & Hoshino 2001, 2007; Jaroschek, Lesch & Treumann 2004; Bessho & Bhattacharjee 2005, 2007, 2010, 2012; Daughton & Karimabadi 2007; Hesse & Zenitani 2007; Lyubarsky & Liverts 2008; Cerutti et al. 2012; Sironi & Spitkovsky 2014; Guo et al. 2014, 2015; Liu et al. 2015; Nalewajko et al. 2015; Sironi, Petropoulou & Giannios 2015; Kagan, Nakar & Piran 2016; Werner et al. 2016) and three dimensions (3D; e.g. Zenitani & Hoshino 2005, 2008; Yin et al. 2008; Liu et al. 2011; Sironi & Spitkovsky 2011b, 2012; Kagan, Milosavljević & Spitkovsky 2013; Cerutti et al. 2014; Sironi & Spitkovsky 2014; Guo et al. 2015). Recently, 2D PIC simulations have started to tackle the dynamics and acceleration capabilities of relativistic reconnection in electron–ion plasmas (e.g. Melzani et al. 2014; Sironi et al. 2015; Guo et al. 2016).

PIC simulations can now reliably simulate the reconnection region, measure the reconnection speed and identify the mechanisms of particle acceleration (see Kagan et al. 2015 for a review). Yet, the separation between the microscopic plasma scales that PIC simulations need to resolve and the large astrophysical scales where the emission takes place is often precluding a direct application of PIC findings to astrophysical observations. It is only when PIC studies are performed with a domain much larger than the microscopic plasma scales, that the results can be properly employed to model astrophysical sources. With large-scale simulations, Sironi & Spitkovsky (2014, hereafter SS14) have shown that non-thermal particle acceleration is a generic by-product of the long-term evolution of relativistic reconnection, in both 2D and 3D, and that the accelerated particles populate a power law whose slope is harder than -2 for magnetizations $\sigma \gtrsim 10$. With large-scale PIC simulations, we have demonstrated that reconnection can satisfy all the basic conditions for the high-energy emission from blazar jets (Sironi et al. 2015, hereafter SPG15): efficient dissipation, extended particle distributions and rough equipartition between particles and magnetic field in the emitting region.

In this work, we employ a suite of large-scale 2D PIC simulations in electron–positron plasmas to follow the evolution of the reconnection layer to unprecedentedly long temporal and spatial scales, so we can capture the asymptotic physics independently of the initial setup of the current sheet. Earlier works were often limited to small domains, nearly one order of magnitude smaller than what we employ here. As a result, transient effects that depended on the initialization of the current sheet were artificially overemphasized, while particle distributions did not have sufficient time to isotropize (e.g. Cerutti et al. 2013), or particle acceleration to the highest energies was artificially inhibited (e.g. Werner et al. 2016). Also, the common choice of periodic boundary conditions in the outflow direction (as opposed to the absorbing/outflow boundary conditions that we employ here) limited the time that these simulations could run before the reconnection process was choked, which resulted in underestimating the terminal speed of the reconnection outflow (e.g. Guo et al. 2015).

With our large-scale simulations, we investigate the properties of the chain of plasmoids/magnetic islands that are constantly generated in the reconnection layer by the secondary tearing instability (Uzdensky, Loureiro & Schekochihin 2010), as a self-consistent by-product of the system evolution. We argue that such plasmoids play the role of the 'blobs' that are commonly invoked in phenomenological models of relativistic astrophysical jets, i.e. quasi-spherical emission regions containing relativistic particles and magnetic fields. We show that the plasmoids are indeed in rough energy equipartition between particles and magnetic fields (with kinetic and magnetic energy densities proportional to the magnetization σ), and that the upper energy cutoff of the plasmoid particle spectrum is proportional to the plasmoid width w, corresponding to a Larmor radius $\sim 0.2\,w$.

By following each individual plasmoid over time, we find that their life can be separated into two phases: first they grow, then they go. The plasmoids grow in size at ~ 0.1 of the speed of light (roughly half of the reconnection inflow rate), with most of the growth happening while they are still non-relativistic; their growth is suppressed once they get accelerated to relativistic speeds by the field line tension, up to the terminal four-velocity $\sim \sqrt{\sigma}\,c$ expected from analytical models (Lyubarsky 2005). The largest plasmoids, occurring every $\sim 2.5\,L/c$, reach a characteristic size $w^{\mathrm{max}} \sim 0.2\,L$ independently of the system length L, they have nearly isotropic particle distributions and they contain the highest energy particles, whose Larmor radius is $\sim 0.03\,L$. The latter can be regarded as the Hillas criterion (Hillas 1984) for relativistic reconnection.

This paper is organized as follows. In Section 2, we describe the simulation setup and our method for identifying and tracking the plasmoids. In Section 3, we discuss the overall structure of the reconnection layer, whereas Section 4 is devoted to the investigation of the plasmoid properties (i.e. their fluid properties, the particle population that they contain, the plasmoid growth and bulk acceleration). In Section 5, we show how our conclusions depend on the system size L and emphasize the artificial constraints imposed by small computational domains. This will allow us to extrapolate our results from our large-scale PIC simulations to the macroscopic scales relevant for the blazar emission (Petropoulou, Giannios and Sironi 2016). In Section 6, we summarize our findings and describe their astrophysical implications.

2 SIMULATION SETUP

We use the 3D electromagnetic PIC code TRISTAN-MP (Buneman 1993; Spitkovsky 2005) to study relativistic reconnection in pair plasmas. Our simulations employ a 2D spatial domain, but we track all three components of the velocity and of the electromagnetic fields. We investigate the case of antiparallel reconnection, i.e. in the absence of a guide field perpendicular to the alternating fields. The reconnection layer is set up in Harris equilibrium, with the initial magnetic field $\boldsymbol{B}_{\mathrm{in}} = -B_0\,\hat{\boldsymbol{x}}\tanh\left(2\pi y/\Delta\right)$ reversing at $y = 0$ over a thickness Δ that will be specified below.[1] The field strength is parametrized by the magnetization $\sigma = B_0^2/4\pi m n_0 c^2 = (\omega_{\mathrm{c}}/\omega_{\mathrm{p}})^2$, where $\omega_{\mathrm{c}} = eB_0/mc$ is the Larmor frequency and $\omega_{\mathrm{p}} = \sqrt{4\pi n_0 e^2/m}$ is the plasma frequency for the cold electron–positron plasma outside the layer (which is initialized with a small thermal spread of $k_{\mathrm{B}}T/mc^2 = 10^{-4}$). The Alfvén speed is related to the magnetization as $v_{\mathrm{A}}/c = \sqrt{\sigma/(\sigma+1)}$. We focus on the regime $\sigma \gg 1$

---

[1] In this work, we focus on the commonly-studied plane-parallel setup in which the initial field lies in the x–z plane. For more complicated geometries, and in particular for the case of explosive relativistic reconnection driven by large-scale magnetic stresses, see Lyutikov et al. (2016).

Table 1. Physical parameters of the simulations.

σ	$L/c\,\omega_{\rm p}$	$L/r_{0,\rm hot}$	Duration (L/c)
3	1229	720	3.6
10	413	127	14.0
10	826	257	3.6
10	1651	518	3.6
10	3584	1130	3.6
50	3584	505	3.6

We provide the system half-length L in units of both the skin depth $c/\omega_{\rm p}$ (second column), which is resolved with 10 cells, and of the Larmor radius of particles heated/accelerated by reconnection $r_{0,\rm hot} = \sqrt{\sigma}\,c/\omega_{\rm p}$ (third column).

(i.e. $v_{\rm A}/c \sim 1$) of relativistic reconnection, investigating three values of the magnetization: $\sigma = 3$, 10 and 50 (see Table 1). The magnetic pressure outside the current sheet is balanced by the particle pressure in the sheet, by adding a component of hot plasma with overdensity $\eta = 3$ relative to the number density n_0 of cold particles outside the layer. From pressure equilibrium, the temperature of the hot plasma in the sheet is $k_{\rm B}T_{\rm h}/mc^2 = \sigma/2\eta$. The hot particles in the sheet are also initialized with a small drift speed along z (electrons and positrons drifting in opposite directions), so that their electric current compensates the curl of the magnetic field.

We trigger reconnection near the centre of the 2D computational domain, by removing the pressure of the hot particles initialized in the current sheet.[2] This triggers a local collapse of the current sheet, which generates an X-point at the centre of the domain. After this initial perturbation, the system evolves spontaneously, i.e. we study spontaneous reconnection, as opposed to forced (or driven) reconnection. The initial perturbation results in the formation of two 'reconnection fronts' that propagate away from the centre along $\pm\hat{x}$ (i.e. along the current layer), at roughly the Alfvén speed $v_{\rm A} = \sqrt{\sigma/(\sigma+1)}\,c$ (see Section 3). We choose the thickness of the current sheet Δ large enough such that reconnection does not get spontaneously triggered anywhere else in the current layer, outside of the region in between the two reconnection fronts. Taking $r_{0,\rm hot} = \sqrt{\sigma}\,c/\omega_{\rm p}$ as our unit of length, which corresponds to the Larmor radius of particles with energy σmc^2 in the field B_0,[3] the thickness Δ is chosen to be $\Delta \simeq 29\,r_{0,\rm hot}$ for $\sigma = 3$, $\Delta \simeq 22\,r_{0,\rm hot}$ for $\sigma = 10$ and $\Delta \simeq 11\,r_{0,\rm hot}$ for $\sigma = 50$. We have tested that our results are insensitive to the value of Δ as long as it is appreciably larger than $r_{0,\rm hot}$, so that active reconnection stays confined in between the two reconnection fronts.

After one Alfvénic crossing time, the two reconnection fronts reach the x boundaries of the computational box (see Section 3). Here, we have explored two choices of boundary conditions: (i) periodic boundary conditions in the x-direction, so that the particles outflowing from the centre accumulate close to the boundaries, where a large magnetic island is formed; or (ii) absorbing boundary conditions in the x-direction of the reconnection outflow, to mimic an open boundary in which no information is able to propagate back inward (Daughton, Scudder & Karimabadi 2006; Belyaev 2015; Cerutti et al. 2015). The choice (i) of periodic boundary conditions has two disadvantages: the large island contains the particles

that were initialized in the current sheet, so the system still bears memory of the initial conditions; in addition, as the large island grows, the central region where reconnection stays active progressively shrinks, which prevents to study the long-term steady-state evolution of the system. For this reason, we adopt the choice (ii) of absorbing boundary conditions, as soon as the two reconnection fronts reach the boundaries of the box (beforehand, periodic boundaries are used along the x-direction). Even though we only present the results from simulations with absorbing boundaries, we have tested that our main conclusions are the same for both choices of boundary conditions.

In the case of absorbing boundary conditions in x, particles are removed from the simulation when they reach the two x boundaries. In a region of width of 60 cells just inside of the two x boundaries, the electromagnetic fields are set by hand to their initial values (i.e. $\boldsymbol{B}_{\rm in}$ as specified above, and zero electric field). Further in, a finite width absorbing layer (with thickness $\Delta_{\rm abs} = 50$ cells) is implemented, where Maxwell's equations contain an electric and a magnetic conductivity term, so that the fields are damped back to the initial conditions. In the absorbing layer, we solve

$$\frac{\partial \boldsymbol{B}}{\partial t} = -c\nabla \times \boldsymbol{E} - \lambda(x)(\boldsymbol{B} - \boldsymbol{B}_{\rm in}) \tag{1}$$

$$\frac{\partial \boldsymbol{E}}{\partial t} = c\nabla \times \boldsymbol{B} - 4\pi\boldsymbol{J} - \lambda(x)\boldsymbol{E}, \tag{2}$$

where the conductivity $\lambda(x)$ is a function of space within the absorbing layer. To minimize wave reflections off the inner edge of the absorbing layer, we gradually increase the conductivity towards the boundaries: if x_1 is the inner edge of the absorbing layer, the conductivity profile is $\lambda = (4/\Delta_{\rm abs}\delta t)[|x - x_1|/\Delta_{\rm abs}]^3$, where δt is the simulation timestep. Outside of the absorbing layer, $\lambda = 0$.

Along the y-direction of the reconnection inflow, we employ two moving injectors (receding from $y = 0$ at the speed of light along $\pm\hat{y}$) and an expanding simulation box, a technique that we have extensively employed in our studies of relativistic shocks (Sironi & Spitkovsky 2009, 2011a; Sironi et al. 2013) and relativistic reconnection (SS14).[4] The two injectors constantly introduce fresh magnetized plasma into the simulation domain. This permits us to evolve the system as far as the computational resources allow, retaining all the regions that are in causal contact with the initial setup. Such choice has clear advantages over the fully-periodic setup that is commonly employed, where the limited amount of particles and magnetic energy will necessarily inhibit the evolution of the system to long times, and the establishment of a steady state.

We resolve the plasma skin depth with $c/\omega_{\rm p} = 10$ cells, so that the Larmor gyration period $2\pi/\omega_{\rm c} = 2\pi/\sqrt{\sigma}\,\omega_{\rm p}$ is resolved with at least a few timesteps, even for the largest magnetization $\sigma = 50$ that we explore (the numerical speed of light is 0.45 cells timestep^{-1}). We investigate the long-term evolution of reconnection in large-scale computational domains. In the following, we shall call L the half-length of the computational domain along the x-direction, i.e. along the reconnection layer. In units of the Larmor radius of hot particles $r_{0,\rm hot} = \sqrt{\sigma}\,c/\omega_{\rm p}$, the half-length L for our fiducial runs is $L \simeq 720\,r_{0,\rm hot}$ for $\sigma = 3$, $L = 1130\,r_{0,\rm hot}$ for $\sigma = 10$ and $L = 505\,r_{0,\rm hot}$ for $\sigma = 50$ (see Table 1). In units of the plasma skin depth, this amounts to $L/c\,\omega_{\rm p} \simeq 1229$ for $\sigma = 3$, and

---

[2] In essence, the current sheet particles around $x, y \sim 0$ are initialized with a small temperature, rather than $T_{\rm h}$.

[3] If reconnection were to transfer all of the field energy to the particles, the mean particle energy would be $\sim\sigma mc^2/2$. So, our definition of $r_{0,\rm hot}$ corresponds, apart from a factor of 2, to the Larmor radius of the particles heated/accelerated by reconnection.

[4] More precisely, our simulation box expands (via discrete jumps along $\pm\hat{y}$) whenever the two injectors approach its top and bottom boundaries, thus allowing us to save memory.

$L/c/\omega_{\mathrm{p}} \simeq 3584$ for both $\sigma = 10$ and 50. This corresponds to an overall box size along the x-direction (so, for the full length $2L$) of 24 576 cells for $\sigma = 3$ and 71 680 cells for both $\sigma = 10$ and 50.[5] As we show below, such large domains are of paramount importance to reconcile the results of PIC simulations with the analytical theory of relativistic magnetic reconnection by Lyubarsky (2005), and to attain a sufficient dynamic range to separate effects happening on plasma scales from the physics at macroscopic scales $\lesssim L$.

For our reference case of $\sigma = 10$, we investigate the dependence of our results on L, exploring also the cases $L \simeq 127\, r_{0,\mathrm{hot}}$, $L \simeq 257\, r_{0,\mathrm{hot}}$ and $L \simeq 518\, r_{0,\mathrm{hot}}$. We evolve the system up to a few L/c (typically, up to $\simeq 3.6\, L/c$), corresponding to $\sim 95\,000$ timesteps for $\sigma = 3$ and $\sim 270\,000$ timesteps for both $\sigma = 10$ (as regard to our reference case with $L = 1130\, r_{0,\mathrm{hot}}$) and $\sigma = 50$. This is sufficient to study with enough statistics the steady state of the system, which is established after $\sim L/c$, as described below.

We typically employ four particles per cell (including both species), but we have extensively tested that the physics is the same when using up to 64 particles per cell (the tests have been performed for the case with magnetization $\sigma = 10$ and box sizes $L \simeq 127\, r_{0,\mathrm{hot}}$ and $L \simeq 257\, r_{0,\mathrm{hot}}$). In order to reduce noise in the simulation, we filter the electric current deposited to the grid by the particles, effectively mimicking the role of a larger number of particles per cell (Spitkovsky 2005; Belyaev 2015).

2.1 Plasmoid identification and tracking

In this subsection, we describe our technique to identify the plasmoids that are self-consistently generated by reconnection, and to follow individual plasmoids over time. As it is customary in MHD simulations (Fermo, Drake & Swisdak 2010; Huang & Bhattacharjee 2012; Loureiro et al. 2012; Murphy et al. 2013), the O-points at the centre of plasmoids and the X-points in between neighbouring plasmoids are identified in a 2D domain as local maxima and minima of the magnetic vector potential A_z. Apart from a minus sign, A_z also corresponds to the magnetic flux function. Each maximum of A_z identifies the O-point at the centre of a plasmoid. The plasmoid area is defined as the region where the vector potential stays larger that the maximal value of A_z of the two neighbouring X-points (each one corresponding to a local minimum of A_z). In other words, the plasmoid contour corresponds to the equipotential line at the maximal value of A_z of the two neighbouring X-points. It is in this region that we measure the area-averaged properties of individual plasmoids, e.g. their density and magnetic and kinetic energy content. The logitudinal size of the plasmoid (or 'length') is measured along the current sheet (i.e. along x at $y = 0$), whereas its transverse size (or 'width') is measured along a cut in the y-direction taken at the location of the corresponding O-point.

The plasmoid speed is defined as the local bulk velocity at the corresponding O-point. We have verified that an isolated plasmoid (i.e. not undergoing a merger with another plasmoid) moves nearly as a solid body, or equivalently that the electric field in the plasmoid comoving frame nearly vanishes. By knowing the plasmoid speed, we can readily measure the plasmoid properties in the comoving frame. Below, we shall indicate with a subscript 'lab' all the quantities measured in the laboratory frame. Otherwise, we will refer to comoving quantities, with the exception of the spatial locations x and y, the inflow speed v_{in} and the outflow four-velocity Γv_{out},

---

[5] The box size along y increases over time, and at the end, it is comparable or larger than the x extent.

which are always measured in the laboratory frame. Here, the bulk Lorentz factor $\Gamma = (1 - v_{\mathrm{out}}^2/c^2)^{-1/2}$.

By accounting for all the particles belonging to the plasmoid, we can compute the island energy and momentum spectrum, in the laboratory or comoving frame. Below, it will be convenient to have an estimate of the upper cutoff of the comoving momentum spectrum of individual plasmoids, which we measure as follows (see also Bai et al. 2015). If p_i is the particle momentum in a given direction (below, we will primarily consider the positron momentum) measured in the plasmoid comoving frame, we define

$$p_{i,\mathrm{cut}} = \frac{\sum_{\alpha \in P} p_{\alpha,i}^{n_{\mathrm{cut}}}}{\sum_{\alpha \in P} p_{\alpha,i}^{n_{\mathrm{cut}}-1}}, \tag{3}$$

where the sum is extended over all the particles α belonging to the plasmoid P, and the power index n_{cut} is empirically chosen to be $n_{\mathrm{cut}} = 6$. If the momentum distribution takes the form $\mathrm{d}N/\mathrm{d}p_i \propto p_i^{-s} \exp(-p_i/p_0)$ with power-law slope s and exponential cutoff at p_0, then our definition yields $p_{i,\mathrm{cut}} \sim (n_{\mathrm{cut}} - s)\, p_0$. In the plasmoid comoving frame, a residual positron anisotropy might persist in the direction $+z$ of the reconnection electric field (with electrons having the opposite anisotropy). It will then be illuminating to distinguish the momentum spectrum of positrons having $p_z > 0$ from positrons with $p_z < 0$. The cutoffs of the corresponding momentum spectra will be indicated as $p_{+z,\mathrm{cut}}$ and $p_{-z,\mathrm{cut}}$, respectively. The quantity p_{cut} will refer to the cut-off momentum for the total comoving momentum $p = (p_x^2 + p_y^2 + p_z^2)^{1/2}$. It will be convenient to cast the value of the momentum cutoffs in terms of the corresponding Larmor radius in the background field B_0, which will be indicated as $r_{0,\mathrm{cut}} = p_{\mathrm{cut}} c/eB_0$ for the total momentum p_{cut} and as $r_{0i,\mathrm{cut}} = p_{i,\mathrm{cut}} c/eB_0$ for the component along the direction i.

After having identified all the plasmoids in a given snapshot of the simulation, we describe how we follow the temporal trajectory of a given plasmoid, which allows us to assess, e.g. how its growth proceeds over time. In our PIC code, each computational particle has a unique identifier. At any given time, we tag each new plasmoid that has been detected in the reconnection layer with a representative particle, whose Lorentz factor is typically chosen to be $1.2 \leq \gamma_{\mathrm{lab}} \leq 2.5$. This range ensures that we have enough particles to be able to tag each of the plasmoids (as we show below, the plasmoid spectrum starts at mildly relativistic energies), and at the same time, we can be confident that the particle of our choice stays effectively trapped in the plasmoid (as opposed to a high-energy particle that was flying outward from the X-point and happened to lie within the plasmoid area at that particular time). At all subsequent times, the location of the chosen particle will allow us to confidently track the temporal history of the given plasmoid.

At certain times, a single plasmoid might contain two or more of such 'tracer particles.' This is a signature that a plasmoid merger has just occurred, and we can uniquely identify which plasmoids have been taking part in the merger event. The post-merger plasmoid will inherit the identifier from the largest of the pre-merger plasmoids (and inherit its corresponding tracer particle), while all the other pre-merger plasmoids will terminate their life history.

3 STRUCTURE AND EVOLUTION OF THE RECONNECTION LAYER

We describe the evolution of the reconnection layer in our large-scale computational domain, from the initial setup, until it reaches a statistical steady state. We focus on the overall structure of the current sheet, and we emphasize the dependence of the inflow and
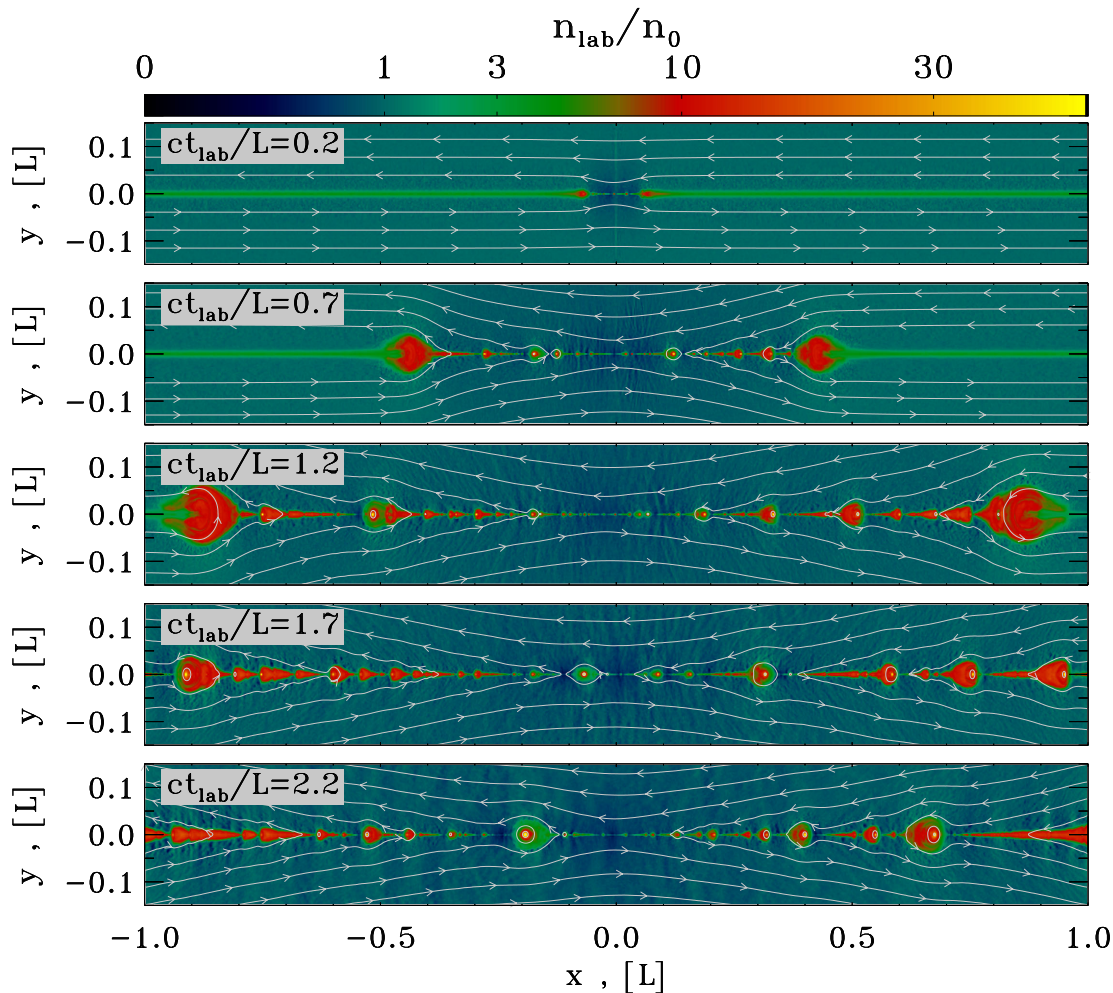
Figure 1. 2D structure of the particle number density in the lab frame $n_{\rm lab}$, in units of the lab-frame number density n_0 far from the reconnection layer, from a simulation with $\sigma = 10$ and $L/r_{0,\rm hot} \simeq 518$. We only show the region $|y|/L < 0.15$ to emphasize the small-scale structures in the reconnection layer (the extent of the computational box along y increases at the speed of light, as described in Section 2). The 2D density structure at different times (as marked on the plots) is shown in the panels from top to bottom, with overplotted magnetic field lines. After triggering reconnection in the centre of the current sheet ($x \simeq 0$ in the top panel), two 'reconnection fronts' propagate to the right and to the left, reaching the boundaries of the box right after $ct_{\rm lab}/L = 1.2$ (see the two overdense regions at $x \simeq -0.4\,L$ and $x \simeq 0.4\,L$ in the second panel, or at $x \simeq -0.85\,L$ and $x \simeq 0.85\,L$ in the third panel). The evolution of the reconnection layer after this time is completely independent of the initialization of the current sheet.

outflow speeds on the flow magnetization, demonstrating excellent agreement of the results of our PIC simulations with the analytical model by Lyubarsky (2005).

3.1 Towards a steady state

Fig. 1 illustrates the early phases of evolution of the system, presenting the 2D structure of the particle number density in the lab frame $n_{\rm lab}$ for a representative case with magnetization $\sigma = 10$ and size $L/r_{0,\rm hot} \simeq 518$. We only show the region $|y|/L < 0.15$ closest to the current sheet, to emphasize the small-scale structures in the reconnection layer; the full extent of our computational box along y is much larger, since it increases with time at the speed of light, as described in Section 2. As anticipated in Section 2, the reconnection process is initiated by hand at the centre of the domain, by removing the thermal pressure of the hot particles in the current sheet near $x, y \sim 0$. Our choice of driving the reconnection onset near the centre – rather than periodically modulating the magnetic flux function, or letting the system go unstable via numerical noise

– would mimic the effect of a large-scale curvature of the field lines (over a scale $\sim L$), such that the current sheet is narrower near the centre. The central region is then most likely to go unstable via the tearing mode,[6] and the signal of ongoing reconnection will propagate towards the outer regions (where the current sheet is broader) before they have time to become unstable.

The lack of pressure support in the vicinity of $x, y \sim 0$ resulting from our initial perturbation triggers the collapse of the current sheet (top panel in Fig. 1), with the magnetic field lines that begin to get advected towards the centre (the magnetic field lines are overplotted in grey in Fig. 1) where an X-point is formed. In the following, we indicate this X-point as the 'primary X-point.' The primary X-point remains in the vicinity of $x \sim 0$ throughout the timespan of our simulations (deviating at most by $\sim 0.2\,L$), and it will be easy to

---

[6] For an unperturbed pair plasma that goes unstable via the tearing instability (seeded by numerical noise), the growth time of the fastest growing mode increases with the current sheet thickness as $\Delta^{5/2}$ (e.g. Zenitani & Hoshino 2007), at fixed magnetization σ and overdensity η.

identify by tracking the large-scale convergence of the field lines, or the divergence of the outflowing plasma velocity.

On the two sides of the primary X-point, two 'reconnection fronts' are formed (see the overdense regions at $|x|/L \sim 0.1$ in the top panel of Fig. 1). Pulled by the tension force of the magnetic field lines, the two reconnection fronts move towards the ends of the current sheet at the Alfvén speed, which, for relativistic reconnection, approaches the speed of light (for the case of $\sigma = 10$ in Fig. 1, the Alfvén speed is $v_A/c \simeq 0.95$). As they propagate, they sweep up the hot plasma that was initialized in the current sheet, so the 'heads' of the two reconnection fronts become wider and wider with time (compare the overdense structures at $|x|/L \sim 0.4$ for $ct_{lab}/L \sim 0.7$ with those at $|x|/L \sim 0.85$ for $ct_{lab}/L \sim 1.2$). After the two reconnection fronts exit through the two absorbing x boundaries of the box (for the case in Fig. 1, this happens around $ct_{lab}/L \sim 1.4$), the system retains no memory of the initialization of the current sheet (in contrast, in the case of periodic boundary conditions in the x-direction, the initial current sheet plasma would accumulate within a large island at the boundary of the box, see Section 2). After the two reconnection fronts have left the domain, the system approaches a statistical steady state (compare the two bottom-most panels in Fig. 1). Even though our main results do not depend on the choice of boundary conditions along the x-direction (absorbing or periodic), it is only when we employ absorbing/outflow boundaries that we can study the steady state of the system for several Alfvén crossing times.

For our choice of a thick current sheet (i.e. $\Delta \gg r_{0,hot}$), the region in between the two reconnection fronts is the only portion of the domain where reconnection is active. In fact, we specifically choose the value of Δ such that reconnection does not spontaneously start anywhere in the region ahead of the two reconnection fronts, during the time it takes for the two fronts to reach the boundaries of the box. In contrast, in the case of a thinner current sheet, the tearing instability would periodically break the initial current layer into a series of magnetic islands, separated by X-points (e.g. see fig. 1a in SS14). Such magnetic islands – which we would call 'primary islands' – would still bear memory of the initialization of the current sheet, since their core has a negligible magnetic content (e.g. see fig. 2c in SPG15) and it is entirely supported by the pressure of the hot particles initialized in the current sheet[7] (see Nalewajko et al. 2015, for an investigation of the structure of primary islands). For our choice of a thick current sheet, no primary islands are formed in the reconnection layer.

The focus of our work is not on primary islands, since their properties would still be sensitive to the details of the current sheet initialization, which would be impossible to constrain from astrophysical observations. Rather, we investigate the properties of the 'secondary islands' resulting from the secondary tearing instability discussed by Uzdensky et al. (2010). Secondary plasmoids are continuously generated in between the two reconnection fronts (or in the whole domain, after the two reconnection fronts have exited the computational box) and then advected outwards by the tension force of the magnetic field lines (e.g. the plasmoid that was located at $x/L = -0.5$ for $ct_{lab}/L = 1.2$ has moved to $x/L = -0.9$ for $ct_{lab}/L = 1.7$). Secondary plasmoids are a self-consistent by-product of the long-term evolution of the system (see Daughton & Karimabadi 2007,

for similar conclusions in non-relativistic reconnection), and their properties only depend on the flow conditions far from the current sheet, i.e. only on the magnetization σ, for our case of antiparallel reconnection in pair plasmas. This allows robust predictions to be made on the observational implications of relativistic reconnection in pulsar winds and jets of blazars and GRBs.

When two plasmoids merge, a current sheet forms in between, along the y-direction. Similarly to the picture described above, this current sheet results in a second generation of secondary plasmoids moving in the y-direction. Further mergers between these plasmoids gives a third generation of secondary plasmoids in the x-direction, with a fractal framework that is expected to continue down to microscopic plasma scales. In this work, we only focus on the first generation of secondary plasmoids, but we expect that our results are equally applicable to all subsequent generations. The only caveat is that, while the plasma flowing into the first-generation current sheet is cold, in all subsequent phases, the inflowing plasma (which already belongs to a 'parent' plasmoid) is relativistically hot.

3.2 The steady-state reconnection layer

The continuous formation and ejection of secondary plasmoids characterizes the steady-state appearance of the reconnection layer, which is presented in Fig. 2 at $ct_{lab}/L = 3.2$ for the same simulation as in Fig. 1. We plot the 2D structure of various quantities, as measured in the lab frame of our simulations. In Section 4, we will quantify how the comoving density and magnetic and kinetic energy content of the secondary plasmoids depend on the plasmoid size. The secondary plasmoids appear as overdense structures (Fig. 2a) containing strong fields (Fig. 2b) and hot particles (Fig. 2c). Fig. 2(b) shows that the cores of secondary plasmoids are significantly magnetized, in contrast with the structure of primary plasmoids (see fig. 1 c in SS14), whose core would be populated by the unmagnetized hot particles that were initialized in the current layer. In the centre of secondary plasmoids, the magnetic and kinetic densities are roughly comparable, i.e. secondary plasmoids are nearly in equipartition of magnetic and kinetic energy (see SPG15, and also Section 4 below). At the centre of the plasmoids, the magnetic energy fraction reaches $\epsilon_{B,lab} = B_{lab}^2/8\pi n_0 \, mc^2 \sim 100$. This should be compared with the value expected in the inflow region, where $\epsilon_{B,lab} \sim \sigma/2 = 5$. So, the magnetic field in the plasmoid core is compressed by a factor of ~ 4, with respect to the initial B_0.

The magnetic field strength is nearly uniform in the inflow region, with the exception of a few areas with weaker fields (in blue in Fig. 2 b; see e.g. at $x/L \sim 0.1$ and $|y|/L \lesssim 0.05$). Such regions lie close to the current sheet, in the vicinity of a large secondary island (for the case indicated above, see the island at $x \sim 0$). As the magnetic field lines advect into the current sheet during the reconnection process, they wrap around large magnetic islands. The same bundle of field lines that are now accumulating on the outskirts of a large island have to make their way to the current sheet, on the two sides of the large island. It follows that the density of field lines near a large magnetic island will be reduced, resulting in weaker fields. In view of flux freezing, this will also correspond to a locally lower value of the number density of inflowing particles (e.g. see the same region at $x/L \sim 0.1$ and $|y|/L \lesssim 0.05$ in Fig. 2a). As we demonstrate in Section 4, this will have implications for the magnetic energy content of small plasmoids, that reside in regions where the inflowing magnetic field is weaker.

The inflow rate of particles is nearly uniform along the current sheet, as shown by the plot of the inflow velocity $v_{in}/c = \boldsymbol{v}/c \cdot \hat{\boldsymbol{y}}$ in Fig. 2(d). The only exceptions are the regions just ahead of the

---

[7] Similar conclusions would hold in the case that the current sheet is set up as a force-free layer (e.g. Guo et al. 2014), rather than a Harris sheet. In such a case, the island cores would be dominated by the pressure of the out-of-plane field initially present in the current sheet.
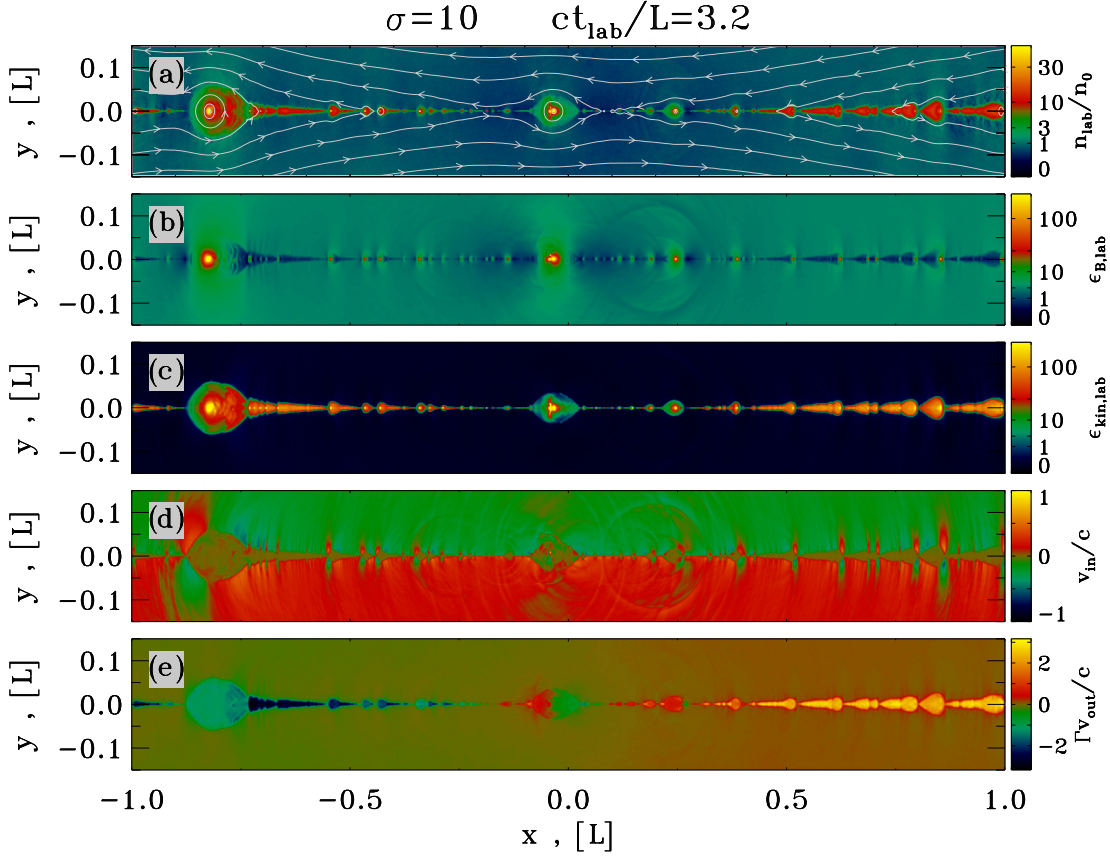
Figure 2. 2D structure of the reconnection layer at $ct_{lab}/L = 3.2$, from a simulation with $\sigma = 10$ and $L/r_{0,hot} \simeq 518$. Along the y-direction, we only show the region $|y|/L < 0.15$ to emphasize the small-scale structures in the reconnection layer (the extent of the computational box along y increases at the speed of light, as described in Section 2 and shown in the animation linked below). From the top to the bottom panel, we show: (a) the particle number density in the lab frame n_{lab}, in units of the number density n_0 far from the reconnection layer, with overplotted magnetic field lines; (b) the magnetic energy fraction $\epsilon_{B,lab} = B_{lab}^2/8\pi n_0\,mc^2$, where the magnetic field B_{lab} is measured in the lab frame; (c) the kinetic energy fraction $\epsilon_{kin,lab} = (\langle\gamma\rangle_{lab} - 1)\,n_{lab}/n_0$, where $\langle\gamma\rangle_{lab}$ is the mean particle Lorentz factor in the lab frame; (d) the inflow bulk speed $v_{in} = \boldsymbol{v}\cdot\hat{\boldsymbol{y}}$ in units of the speed of light; (e) the outflow bulk four-velocity $\Gamma v_{out} = \Gamma\,\boldsymbol{v}\cdot\hat{\boldsymbol{x}}$ in units of the speed of light. The reconnection layer is fragmented into a series of overdense magnetized hot plasmoids, which are propagating away from the centre at ultra-relativistic speeds. The inflow speed (i.e. the reconnection rate) is mildly relativistic ($v_{in}/c \sim 0.1$), and remarkably uniform along the current sheet. [The animation referring to Fig. 2 is available as supporting information.]

secondary plasmoids, where the plasmoids plunge into the inflowing plasma and they push it aside (see e.g. to the left of the plasmoid at $x/L \sim -0.8$ in Fig. 2d, where v_{in} has opposite sign than in the bulk of the inflow). The inflow speed is non-relativistic, $v_{in}/c \sim 0.15$. In Lyubarsky (2005)'s analytical model of relativistic reconnection, the inflow speed is closely related to the opening angle θ of the magnetic field in the inflow region (with respect to the x-axis), with $v_{in}/c = \tan\theta$. From Fig. 2(a), the inclination of the magnetic field lines is such that $\tan\theta \sim 0.15$, which is in excellent agreement with the inflow speed that we measure in Fig. 2(d). In steady state, both the obliquity of the field lines and the inflow velocity (or 'reconnection rate') stay remarkably constant in time.

The 2D plot in Fig. 2(d) also reveals the presence of spherical waves propagating back into the inflow region (e.g. see the spherical front centred at $(x, y) \sim (0.2, 0)\,L$). They appear most clearly in the plots of inflow velocity (Fig. 2d) and magnetic energy fraction (Fig. 2b), and they are generated by the merger event of two plasmoids. Plasmoid mergers are rather frequent, as a result of the fact that different plasmoids propagate at different speeds along the layer, with larger plasmoids typically moving slower. Fig. 2(e) presents the structure of the outflow bulk four-velocity $\Gamma v_{out} = \Gamma\,\boldsymbol{v}\cdot\hat{\boldsymbol{x}}$, in units of the speed of light. The large plasmoid

at $x/L \sim -0.8$ moves slower than the smaller plamoids in its wake, which will eventually accrete on to the large plasmoid, further increasing its mass. In addition to such 'minor mergers' between plasmoids of unequal sizes, occasional 'major mergers' of equal-mass plasmoids might occur, as it is happening in the central region of Fig. 2(e). The convergence of the velocity flow in between merging plasmoids is believed to play an important role for particle acceleration (Drake et al. 2006; Guo et al. 2014, 2015; SS14; Nalewajko et al. 2015). The dependence of the plasmoid speed on its size will be extensively quantified in Section 4. Yet, Fig. 2(e) already suggests that, while large islands exit the layer with only trans-relativistic velocities, small plasmoids can reach ultra-relativistic speeds. Small plasmoids approach the terminal four-velocity $\Gamma v_{out}/c \sim \sqrt{\sigma} \sim 3.3$ expected for the bulk outflow from relativistic $\sigma = 10$ reconnection (Lyubarsky 2005).[8]

In Fig. 3, we demonstrate that the predictions of Lyubarsky (2005)'s theory, as regard to the inflow and outflow speeds in

[8] We remind that Lyubarsky (2005)'s predictions on the bulk outflow speed from relativistic reconnection are based on a steady-state model of the reconnection layer, i.e. neglecting its fragmentation into plasmoids.
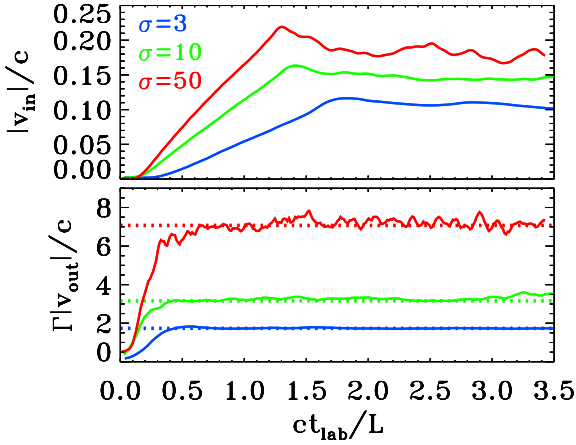
Figure 3. Inflow and outflow speeds as a function of time in the lab frame, for three values of the magnetization σ, as indicated in the legend of the top panel ($\sigma = 3$ in blue, $\sigma = 10$ and $L \simeq 518\,r_{0,\text{hot}}$ in green, and $\sigma = 50$ in red). Top panel: inflow bulk speed in units of the speed of light, averaged over a region of width $|y| \lesssim 0.5\,L$ across the reconnection layer (but our results are nearly independent of this choice). The steady-state inflow speed, after the two reconnection fronts have exited the computational domain (i.e. at $ct_{\text{lab}}/L \gtrsim 1.5$), has a weak dependence on the magnetization. Bottom panel: maximum outflow four-velocity, in units of the speed of light. For each value of the magnetization, we take the slice at $y = 0$ and plot the fifth largest value of the ouflow four-velocity (but we have tested that the variation from the first largest to the 10th largest is minimal). The resulting peak outflow four-velocity in in excellent agreement with the prediction $\Gamma\,|v_{\text{out}}|/c \sim \sqrt{\sigma}$ by Lyubarsky (2005), indicated by the dotted lines.

relativistic reconnection, hold for the whole range of magnetizations $\sigma = 3$–50 explored in our work. In the top panel, we present the inflow bulk speed in units of the speed of light, averaged over a region of width $|y| \lesssim 0.5\,L$ along the y-direction and extending along the whole current sheet in the x-direction. The top panel in Fig. 3 shows that, after the system reaches a steady state (i.e. at $ct_{\text{lab}}/L \gtrsim 1.5$), the inflow speed (or equivalently, the reconnection rate) has only a weak dependence on the magnetization, varying from $|v_{\text{in}}|/c \sim 0.10$ for $\sigma = 3$ up to $|v_{\text{in}}|/c \sim 0.18$ for $\sigma = 50$. The weak dependence of the inflow speed on the magnetization is consistent with earlier works (SS14; Guo et al. 2015) and with the analytical model of Lyubarsky (2005), that predicted that the reconnection rate should saturate in the limit $\sigma \gg 1$ at a value around $\sim 0.1\,c$. The inflow speeds presented in Fig. 3 are obtained by averaging over a macroscopic region of size $2\,L \times L$, and are therefore representative of the mean dissipation rate of the magnetic field. The value of the inflow speed can be much larger in the vicinity of X-points, approaching the speed of light (e.g. Liu et al. 2015), but such large values only extend over microscopic skin-depth scales.

The inflow speeds presented in the top panel of Fig. 3 are about a factor of 2 larger than we reported in SS14, just due to a different choice of the area where we average the inflow rate. In SS14, reconnection proceeded from numerical noise, resulting in the formation of a number of primary plasmoids. The inflow speed nearly vanished at the location of the primary plasmoids, whereas in between primary plasmoids, it resembled the values presented in Fig. 3. At any given time, about half of the current sheet length was occupied by primary plasmoids. By averaging over the entire domain (and not just over the active regions in between primary plasmoids), we then obtained a value that is indeed expected to be half of what we quote here.

The linear increase in the inflow speed at early times ($ct_{\text{lab}}/L < 1.5$) is simply driven by the fact that the distance between the two reconnection fronts is progressively increasing, as they move from the centre towards the boundaries of the box. As we have explained above, it is only in the region in between the two fronts that the reconnection process is active. At all times, the inflow velocity in between the two fronts is the same as the steady-state value that we read from the top panel of Fig. 3 at late times ($ct_{\text{lab}}/L \gtrsim 1.5$). Ahead of the two reconnection fronts, the plasma is still at rest. One would then expect that the reconnection rate presented in the top panel of Fig. 3, which is averaged over the whole extent of the current sheet, would increase linearly from zero up to the steady-state value, as the two fronts move outward at nearly the Alfvén speed. The time for the two fronts to propagate to the boundaries of the box is $\sim L/v_A$, which explains why it takes slightly longer for $\sigma = 3$, where $v_A \simeq 0.85$, than for $\sigma = 10$ and 50, where the Alfvén speed is nearly the speed of light.

While the inflow speed in relativistic reconnection is non-relativistic, the outflowing plasma can reach ultra-relativistic velocities. This is illustrated in the bottom panel of Fig. 3, where we present the maximal value of the outflow four-velocity $\Gamma\,|v_{\text{out}}|/c$ as a function of time.[9] For all the magnetizations we explore, the peak outflow four-velocity is in excellent agreement with the prediction $\Gamma\,|v_{\text{out}}|/c \sim \sqrt{\sigma}$ by Lyubarsky (2005), which is indicated by the dotted lines (the colour coding is described in the legend in the top panel). Or equivalently, the outflow velocity approaches the Alfvén speed $v_A/c = \sqrt{\sigma/(\sigma + 1)}$. This conclusion also holds in the case of periodic boundary conditions, as long as the computational box is sufficiently large (as argued in SS14).

The box length needed to capture the asymptotic value of $\Gamma\,|v_{\text{out}}|/c$ can be estimated from the early increase in the curves in the bottom panel of Fig. 3. This shows that the outflow accelerates to the terminal speed on a time-scale that is shorter than the Alfvén crossing time of the box, yet not much shorter. For the most extreme magnetization of $\sigma = 50$ (red curve), the acceleration time is $\sim 0.4\,L/c$. Since the overall box length in this case is $2L \sim 1000\,r_{0,\text{hot}}$, we argue that a simulation, whose x extent is smaller than $\sim 400\,r_{0,\text{hot}}$, would not be able to capture the terminal outflow speed of $\sigma = 50$ reconnection. While this estimate is appropriate for the case of absorbing (or outflow) boundary conditions, in the case of periodic boundaries, the same requirement should be imposed over the distance in between two neighbouring primary islands, resulting in a much more constraining condition on the overall box length (which typically includes many primary plasmoids). This might explain why earlier works (Cerutti et al. 2013; Guo et al. 2015; Kagan et al. 2016) claimed that the outflow speed from relativistic reconnection seems systematically lower than Lyubarsky (2005)'s prediction. With a sufficiently large domain, we are able to demonstrate that the outflow four-velocity from relativistic reconnection can be as fast as $\sim\sqrt{\sigma}\,c$, in full agreement with Lyubarsky (2005)'s model.

4 THE PLASMOID CHAIN

In this section, we focus on the chain of secondary plasmoids that are continuously generated in the reconnection layer as a result of the secondary tearing instability (Uzdensky et al. 2010). As a function of

---

[9] The maximal value plotted in Fig. 3 is defined as the fifth largest value of $\Gamma\,|v_{\text{out}}|/c$ computed along the 1D slice at $y = 0$, but we have tested that the variation from the first largest to the 10th largest is minimal.
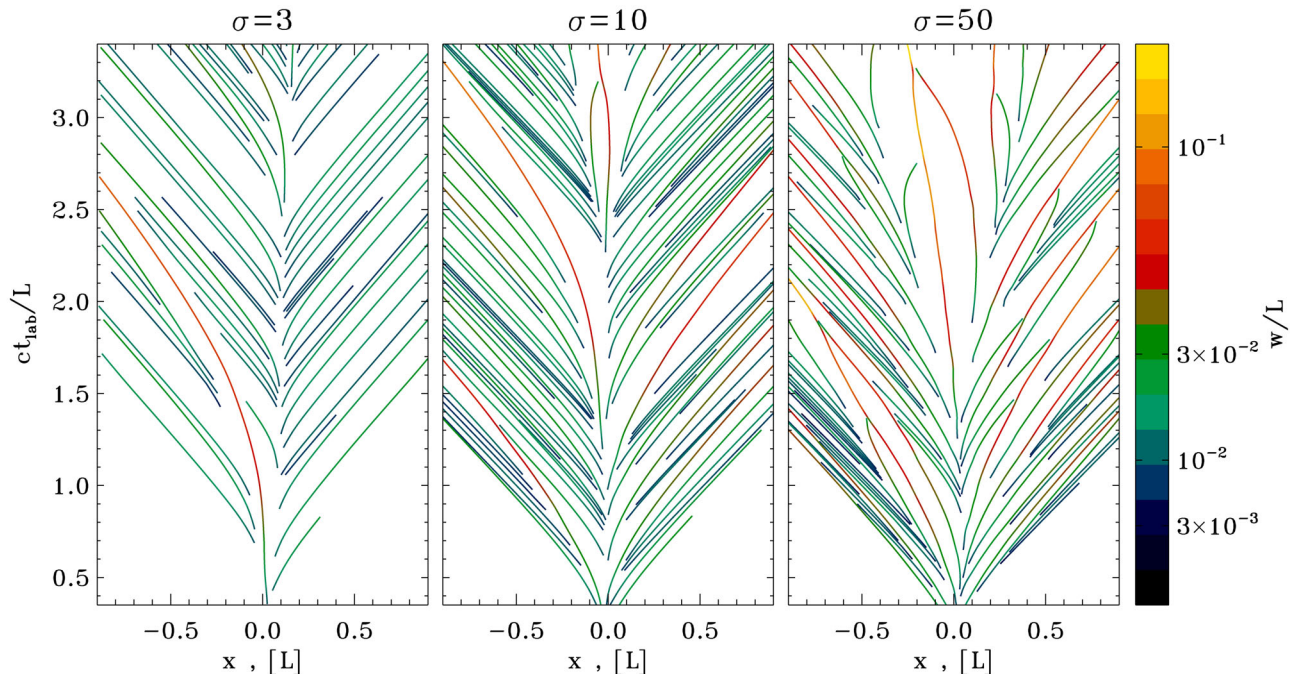
Figure 4. Position–time diagram of magnetic islands, for three values of the magnetization, as indicated at the top ($\sigma = 3$ in the left-hand panel, $\sigma = 10$ and $L/r_{0,\mathrm{hot}} \simeq 518$ in the middle panel, and $\sigma = 50$ in the right-hand panel). The islands start from the centre of the layer ($x \simeq 0$), where reconnection is initially triggered, and while propagating outwards, they grow in size (as indicated by the colours, the plasmoid width w is in units of the system length L) and they accelerate, approaching the speed of light (which would correspond to lines oriented at $45°$ in the plots). Their tracks terminate when they either leave the reconnection layer at $|x| = L$ or they merge with a bigger plasmoid, as it frequently happens at large magnetizations. For the sake of clarity, we only plot the evolutionary tracks of plasmoids whose lifetime (in the lab frame) is longer than $\simeq 0.35L/c$.

their size, in Section 4.1, we quantify their fluid properties (averaged over the plasmoid volume), and in Section 4.2, the spectrum and anisotropy of the particle population that they contain. We also follow individual plasmoids over time, quantifying their growth (in Section 4.3) and acceleration (in Section 4.4) as they propagate from the centre towards the boundaries.

Fig. 4 presents the position–time diagram of secondary plasmoids, for the three values of magnetization that we explore in this work ($\sigma = 3$ on the left, $\sigma = 10$ in the middle and $\sigma = 50$ on the right). The various tracks follow the trajectories of individual plasmoids (more precisely, of their centre), as they move along the reconnection layer. The plasmoid width w in the direction transverse to the current sheet is indicated by the colour scale on the right (red and yellow for the largest plasmoids). For the sake of clarity, we only plot the evolutionary tracks of plasmoids whose lifetime (in the lab frame) is longer than $\simeq 0.35L/c$.

For all the values of magnetization we explore, we see that the vicinity of the primary X-point, where reconnection is initially triggered, is always a preferred region for the formation of long-lived secondary plasmoids. They form around the centre with an initial width of a few plasma skin depths, and as they propagate outwards, they grow in size, as indicated by the colours (e.g. see the plasmoid that for $\sigma = 3$ starts in the centre at $ct_{\mathrm{lab}}/L \sim 0.4$ and exits to the left at $ct_{\mathrm{lab}}/L \sim 2.7$). In general, the longer they spend around the central region, the bigger they grow. Eventually, the tension force of the magnetic field accelerates them outwards, with the fastest plasmoids approaching the Alfvén speed. Since for all the cases explored in this work, the Alfvén speed is close to the speed of light (with the only marginal exception of $\sigma = 3$, that gives $v_A \simeq 0.85\,c$), plasmoids moving at the Alfvén speed would have position—time tracks oriented at $\pm 45°$ in Fig. 4, as indeed is observed for most of the small

plasmoids (as we show in Section 4.4, at a given distance from the centre, larger plasmoids always move slower than smaller ones).

Even though most of the plasmoids shown in Fig. 4 start from the central region, copious production of secondary islands occurs everywhere in the reconnection layer (see also Fig. 2). For example, the relatively large plasmoid that exits to the left at $ct_{\mathrm{lab}}/L \sim 2.7$ for $\sigma = 3$ is preceded by a series of smaller plasmoids, all generated at a distance of $\gtrsim 0.2\,L$ from the centre, and in some cases even further out. Plasmoids generated close to the boundaries exit the domain before reaching the threshold lifespan of $\simeq 0.35L/c$ adopted in Fig. 4, so they do not appear in the figure.

The plasmoid trajectories in Fig. 4 terminate when either the plasmoid exits one of the two boundaries or it merges with a bigger plasmoid. For example, the small plasmoids that, in the left-hand panel, are trailing the large plasmoid mentioned above will terminate their life by merging with it. It follows that smaller plasmoids typically have shorter lives, since they will eventually encounter a bigger plasmoid moving ahead of them (which propagates slower) and merge with it. In addition to such minor mergers (indicated as 'minor' because of the size difference of the two plasmoids), major mergers between plasmoids of comparable widths can also occur, typically close to the centre. This is seen in the case of $\sigma = 50$ (right-hand panel) at $ct_{\mathrm{lab}}/L \sim 3.3$, where two large islands merge at $x \simeq -0.2\,L$. Fig. 4 shows that, in the course of the merger, the width of the two islands shrinks (see the point where the two tracks meet). This is just a consequence of our criterion for the identification of the plasmoid contour, that relies on the maximal value of the vector potential A_z among the two neighbouring X-points (each one being a local minimum of A_z). In a merger, the X-point in between the two islands will have the largest value of A_z, and it will set the plasmoid contours. As the two plasmoids approach in the course

of the merger, the value of A_z in the X-point will increase, so the two contours will shrink more and more, resulting in an apparent decrease of the width of the two islands. Soon after the merger, the surviving plasmoid (the larger of the two) recovers its proper width.

Mergers are most frequent at higher magnetizations. The total electric current in a plasmoid of a given size scales as $\propto \sqrt{\sigma}w$,[10] which results in a stronger interaction among neighbouring plasmoids for higher magnetizations, and a consequent increase in the merger rate. Indeed, while in the case of $\sigma = 3$ (left-hand panel), mergers predominantly involve smaller (so, faster) plasmoids catching up with larger (so, slower) islands, the situation is much more diverse in the high-magnetization case $\sigma = 50$ (right-hand panel). There, it is quite frequent that large plasmoids merge both with trailing plasmoids (for the large plasmoid exiting on the left at $ct_{\mathrm{lab}}/L \sim 2.1$, see the merger at $x/L \sim -0.7$ and $ct_{\mathrm{lab}}/L \sim 1.9$) and with leading plasmoids that are pulled back by the attractive force of the large plasmoid (for the same plasmoid, see the merger at $x/L \sim -0.5$ and $ct_{\mathrm{lab}}/L \sim 1.4$). In the latter case, the leading plasmoid that is pulled back might even reverse its velocity along the layer.

The high merger rate in high-σ flows has two main consequences. First, the spherical waves emanating from each merger event (e.g. see Fig. 2d) will seed fluctuations in the current sheet, triggering the formation of additional secondary plasmoids. In fact, we find that, for the same timespan and domain size, high-σ flows result in a much larger number of secondary islands. Secondly, in the high-magnetization case, small plasmoids leading a large island will be decelerated by its attraction (in the extreme limit, to the point of being pulled back and merge with the large plasmoid). This will tend to inhibit their acceleration up to the Alfvén speed. As we show in Section 4.4, for $\sigma = 50$, a smaller number of plasmoids will be able to approach the expected terminal four-velocity $\sqrt{\sigma} c$, as compared to lower magnetizations.

Finally, Fig. 4 suggests that large plasmoids are rarer than smaller plasmoids. At any given time, several small plasmoids can co-exist in the reconnection layer, but only a few large plasmoids. In Section 4.1, we will quantify the plasmoid size distribution. Interestingly, in the right-hand panel of Fig. 4, we notice a clear signature of quasi-periodicity in the ejection time of relatively large plasmoids (with final width between $0.05L$ and $0.1L$). Looking at the plasmoids escaping on the right, we detect an island leaving at $ct_{\mathrm{lab}}/L \sim 1.9$, followed by others of similar size at $ct_{\mathrm{lab}}/L \sim 2.3, 2.6, 3.1$ and 3.3. In Section 4.3, we demonstrate that such a quasi-periodicity also holds for the largest plasmoids generated in the layer, with width $\sim 0.2L$. By following a system with $\sigma = 10$ and $L/r_{0,\mathrm{hot}} \simeq 127$ up to $ct_{\mathrm{lab}}/L \sim 14$, we will show that their typical recurrence time is $\sim 2.5L/c$.

4.1 Plasmoid fluid properties

In Fig. 5, we analyse a number of fluid properties of secondary plasmoids, averaged over the plasmoid volume. We investigate how the plasmoid properties depend on the width w (on the horizontal axis, in units of L) and on the flow magnetization σ (with $\sigma = 3$ in the left-hand column, $\sigma = 10$ in the middle column and $\sigma = 50$ in the right-hand column). Each panel in Fig. 5 is a 2D histogram indicating the number of plasmoids with a given fluid property (for example, a given value of the rest-frame density) and a given width, normalized to the overall number of magnetic islands

N_{isl}. All of the plasmoid properties investigated in Fig. 5 refer to comoving quantities. From quantities measured in the simulation frame, the corresponding comoving values can be easily obtained via Lorentz transformations, since we can measure the velocity of each plasmoid (and consequently, its bulk Lorentz factor Γ). We remark again that, while earlier works focused on the structure of primary plasmoids (Nalewajko et al. 2015), that are necessarily affected by the prescribed setup of the initial Harris sheet, here we study secondary plasmoids, whose properties only depend on the flow magnetization.

The first row of Fig. 5 shows that the plasmoids are quasi-spherical in their rest frame, with a ratio of comoving length $w_{\parallel}$ to width w that lies around ~ 1.5 (as indicated by the dotted white lines in the plot), irrespective of the magnetization σ. The tendency for sphericity is even more pronounced when the plasmoids approach the terminal four-velocity $\sim \sqrt{\sigma} c$. We have also verified that the plasmoid area is well approximated by $\pi w_{\parallel} w/4$, as expected for an ellipse with major axis $w_{\parallel}$ and minor axis w.

The second row of panels shows dependence on w and σ of the average comoving density $n = n_{\mathrm{lab}}/\Gamma$, in units of the particle number density n_0 far from the current sheet. For each value of the magnetization, the comoving number density appears to be nearly independent of the plasmoid size. The density has a weak dependence on magnetization, varying from $n/n_0 \sim 3$ for $\sigma = 3$ up to $n/n_0 \sim 5$ for $\sigma = 50$. This is in apparent disagreement with Lyubarsky (2005)'s theory, predicting that the rest-frame density in the fast outflows from relativistic reconnection should scale as $n/n_0 \sim 2\sqrt{\sigma}$ (as indicated by the dotted white lines). However, Lyubarsky (2005)'s scalings only apply to a fully accelerated smooth outflow (i.e. moving with the Alfvén speed). As we will see in Section 4.4, while most of the plasmoids are successfully accelerated to the Alfvén speed for $\sigma = 3$ (where, in fact, the expected scaling is satisfied), only few plasmoids can reach the terminal four-velocity of $\sim \sqrt{\sigma} c$ for $\sigma = 50$.

We now present a simple argument describing why the scaling $n/n_0 \propto \sqrt{\sigma}$ is only to be expected for the fastest moving plasmoids. Pressure balance across the current sheet, between the pressure of hot particles in the islands and the magnetic pressure of the cold inflow, dictates that the mean plasmoid internal energy fraction should scale as $\epsilon_{\mathrm{kin}} \sim \sigma$ (see also the fifth row of panels in Fig. 5). Here, $\epsilon_{\mathrm{kin}} = (\langle \gamma \rangle - 1)n/n_0$, where $\langle \gamma \rangle$ is the mean comoving particle Lorentz factor. In addition, conservation of the energy per particle requires that $\sigma \sim \Gamma \epsilon_{\mathrm{kin}}/(n/n_0)$, where Γ is the plasmoid bulk Lorentz factor. In reality, the mean energy per particle is likely to be smaller than $\sim \sigma$ during the acceleration phase, since some 'potential energy' is still available in the field line tension, which will only be released when the plasmoid reaches the expected terminal velocity. It follows that we would generally expect $\Gamma \epsilon_{\mathrm{kin}}/(n/n_0) \lesssim \sigma$. Combined with the pressure balance $\epsilon_{\mathrm{kin}} \sim \sigma$, this implies that $n/n_0 \gtrsim \Gamma$, with the equality being realized only for plasmoids moving at the Alfvén speed, or equivalently with $\Gamma \sim \sqrt{\sigma}$.[11] The condition $n/n_0 \gtrsim \Gamma$ is realized for all the plasmoids of our simulations, regardless of the flow magnetization. In particular, we find that the densest plasmoids are typically the fastest ones, fully accelerated up to the Alfvén speed.

The third row of panels in Fig. 5 illustrates the dependence on plasmoid size and magnetization of the magnetic flux Ψ (more specifically, of $\Psi/B_0 w$, since the flux is expected to depend linearly

---

[10] Here, we have assumed that the magnetic field at the plasmoid boundary is always equal to the initial B_0.

[11] In this whole argument, we have implicitly assumed that $\sigma \gg 1$ for the sake of simplicity.
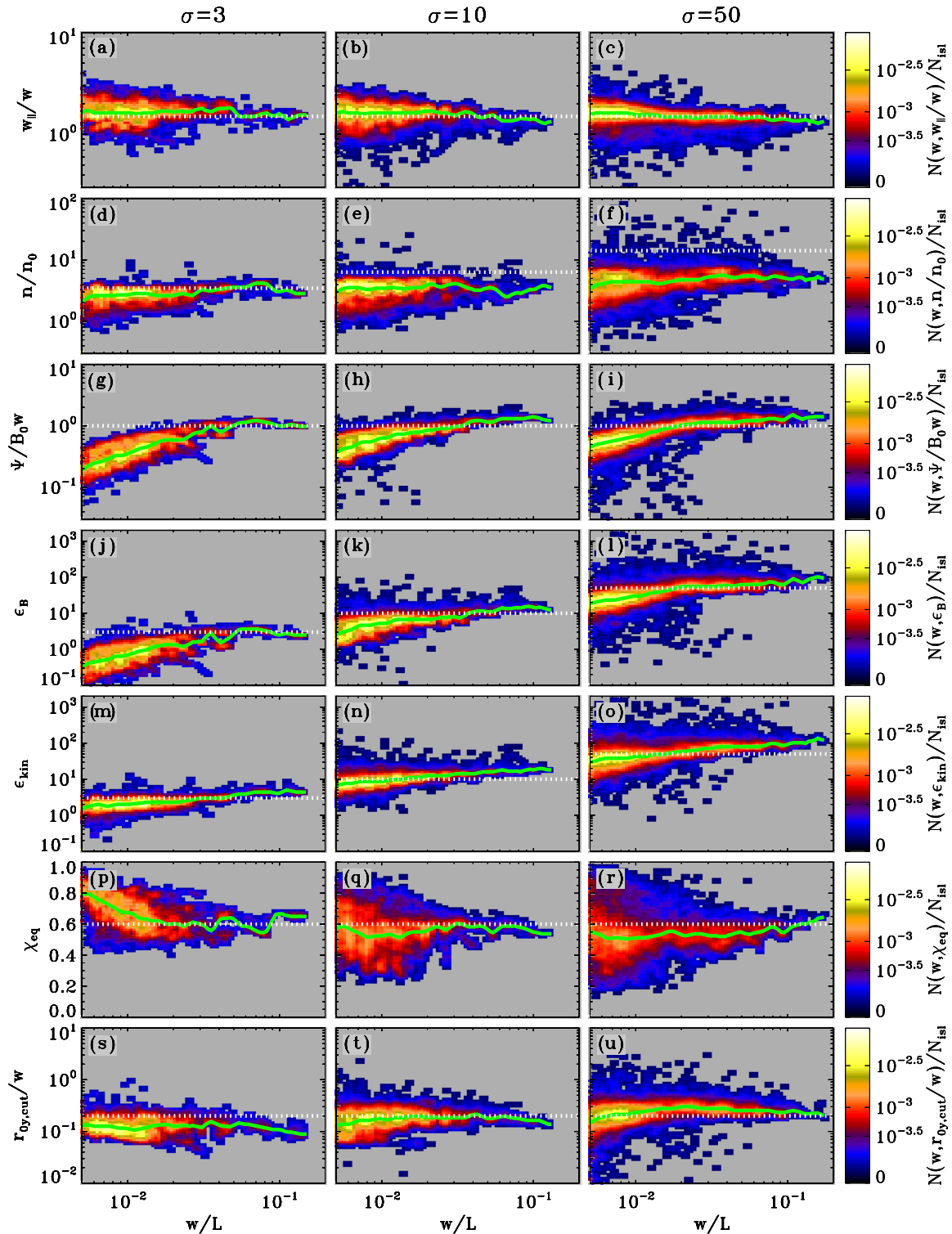
Figure 5. 2D histograms of various plasmoid properties as a function of the width w (in units of L), for three values of the magnetization, as indicated at the top ($\sigma = 3$ on the left, $\sigma = 10$ in the middle, and $\sigma = 50$ on the right). In each bin, the number of plasmoids is normalized to the total number of magnetic islands $N_{\rm isl}$ (see the colour bars on the right). The green solid lines indicate the median values. From top to bottom row, we show: (a)–(c) the ratio of the length $w_\parallel$ (measured in the comoving frame) to the width w, which is around ~ 1.5 regardless of the magnetization (as indicated by the dotted white lines); (d)–(f) the comoving density n averaged over the plasmoid area, in units of the density n_0 far from the current sheet, with the scaling $n/n_0 \sim 2\sqrt{\sigma}$ predicted by Lyubarsky (2005) indicated with the dotted white lines; (g)–(i) the plasmoid flux Ψ, which approaches the nominal value $B_0 w$ at large sizes (see the dotted white lines); (j)–(l) the magnetic energy fraction $\epsilon_{\rm B} = B^2/8\pi n_0 mc^2$ averaged over the plasmoid area, where B is measured in the plasmoid comoving frame; (m)–(o) the internal energy fraction $\epsilon_{\rm kin} = (\langle \gamma \rangle - 1) n/n_0$ averaged over the plasmoid area, where $\langle \gamma \rangle$ is the mean particle Lorentz factor in the plasmoid frame; both $\epsilon_{\rm B}$ and $\epsilon_{\rm kin}$ scale as $\propto \sigma$, as indicated with the dotted white lines; (p)–(r) the equipartition parameter $\chi_{\rm eq}$ as defined in equation (5), which lies around ~ 0.6 regardless of the magnetization, as indicated by the dotted white lines; (s)–(u) the Larmor radius $r_{0y,\rm cut} = p_{y,\rm cut} c / e B_0$ of the positrons at the cut-off momentum $p_{y,\rm cut}$ as defined in equation (3), in units of the plasmoid width; this lies around ~ 0.2 regardless of the magnetization, as indicated by the dotted white lines.
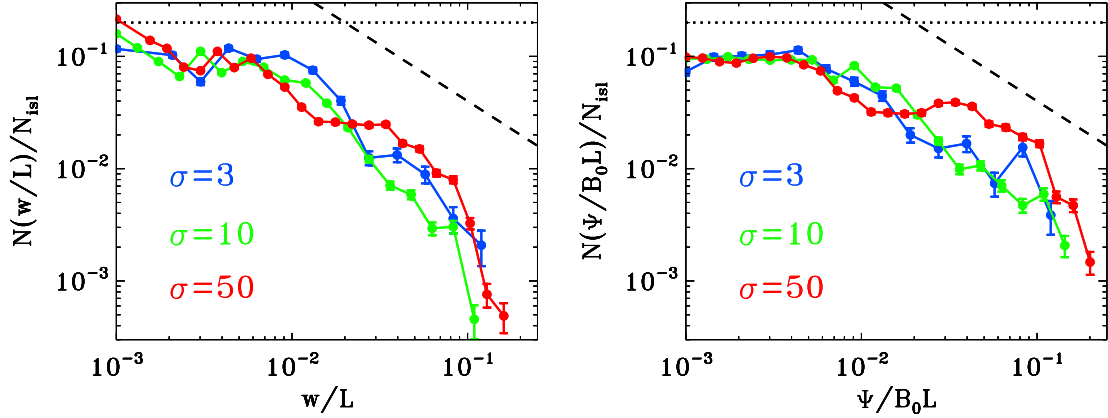
Figure 6. Plasmoid width (left) and flux (right) cumulatives distribution functions, for three values of the magnetization, as indicated in the legend ($\sigma = 3$ in blue, $\sigma = 10$ in green and $\sigma = 50$ in red). The width is normalized to the system length L and the flux to $B_0 L$, while the histogram (with Poissonian error bars) is normalized to the overall number of plasmoids N_{isl}. The corresponding differential distributions can be obtained as $f(w) = \mathrm{d}N(w)/\mathrm{d}w$ and $f(\Psi) = \mathrm{d}N(\Psi)/\mathrm{d}\Psi$. The predictions $N(w) \propto w^{-1}$ by Uzdensky et al. (2010) and Loureiro et al. (2012) and $N(w) \propto$ const by Huang & Bhattacharjee (2012) (and similarly for Ψ) are plotted as dashed and dotted black lines, respectively.

on the plasmoid size). The magnetic flux in a given plasmoid is defined as the difference between the vector potential A_z at the plasmoid O-point and at its contour (which is an equipotential surface). Since A_z is Lorentz invariant, the plasmoid flux is also Lorentz invariant. As expected, we find that at large sizes, $\Psi/B_0 w$ approaches a constant of order unity (as indicated by the dotted white lines). In contrast, at small sizes (typically, $w/L \lesssim 0.02$), the plasmoid flux is systematically lower than the expected value $\sim B_0 w$. As we show below, the same trend is observed for the mean magnetic energy density of small plasmoids.

A similar deficit of magnetic flux at small sizes has been observed in MHD simulations of non-relativistic plasmoid-dominated reconnection (fig. 4 in Loureiro et al. 2012). There, it was attributed to the effect of plasmoid mergers. They envisioned the coalescence as a gradual stripping of the outer layers of the smaller plasmoid, so the magnetic flux in a semidigested plasmoid would be $\Psi \sim B_0 w^2/w_0$, where w_0 is the plasmoid width at the beginning of the merger. Here, we find that the lack of magnetic flux in small plasmoids holds for both merging and non-merging plasmoids. As we have anticipated in Section 3, the inflow region around a relatively large plasmoid generally displays a lower magnetic content (so, $B \lesssim B_0$), as a result of the field lines piling up on the outskirts of the large plasmoid. A small plasmoid lying in the current sheet in the vicinity of a large plasmoid will have a surface magnetic field $B \lesssim B_0$, as we further demonstrate in Appendix A. More precisely, the surface magnetic field is weaker for smaller plasmoids. This justifies the trend in magnetic flux in the third row of Fig. 5.

We have also verified that the transition from $\Psi/B_0 w \lesssim 1$ to $\Psi/B_0 w \sim 1$ always occurs at the same value of w/L, regardless of the system length (i.e. for different choices of $L/r_{0,\text{hot}}$). In fact, as we demonstrate in Section 5, the largest islands always reach a width $w/L \sim 0.1$–0.2, regardless of $L/r_{0,\text{hot}}$. At their surface, the magnetic field is comparable to the field B_0 far from the current sheet. Since the largest islands are controlling the structure of magnetic field lines near the current sheet (magnetic field lines have to wrap around the biggest islands), one would expect that small islands whose width is a fixed fraction of the size of the largest islands will have a similar suppression of the magnetic flux, independent of the system length $L/r_{0,\text{hot}}$. This is indeed what we find.

From the 2D histogram of size and magnetic flux in the third row of Fig. 5, one can find the distribution of plasmoid sizes and

magnetic fluxes, by projecting on to the two axes. Our results are shown in Fig. 6, where we present the cumulative distribution of plasmoid sizes (left-hand panel, with the plasmoid width in units of the system length L) and fluxes (right-hand panel, with the flux in units of $B_0 L$). In the plots, the dashed lines indicate the prediction $N(w) \propto w^{-1}$ by Uzdensky et al. (2010) (and similarly for Ψ), whereas the dotted lines indicate the scaling $N \propto$ const suggested by Huang & Bhattacharjee (2012). The main difference among the two models lies in the assumption on the relative velocity between merging plasmoids, which Uzdensky et al. (2010) took to be always $\sim v_A$, whereas Huang & Bhattacharjee (2012) allowed for a more detailed dependence on the plasmoid size.

Fig. 6 suggests that the plasmoid distributions (for both width and magnetic flux) are nearly the same for the three values of magnetization we investigate in this work ($\sigma = 3$ in blue, 10 in green and 50 in red). In addition, our findings are fully consistent with the results of MHD simulations of non-relativistic and relativistic reconnection (Fermo et al. 2010; Huang & Bhattacharjee 2012; Loureiro et al. 2012; Takamoto 2013). The distributions show a hard slope at small sizes and fluxes (at $w/L \lesssim 0.01$ and $\Psi/B_0 L \lesssim 0.01$), resembling the $N \propto$ const prediction of Huang & Bhattacharjee (2012). This is clearer in the magnetic flux distribution than in the size distribution. Ideally, one would need to extend our study to even larger system lengths in order to attain a broader dynamic range in w and Ψ, and reliably probe the distributions of small islands (for comparison, the MHD study by Huang & Bhattacharjee 2012 extended over six orders of magnitude in Ψ). For the magnetic flux, the break at $\Psi/B_0 L \sim 0.01$ likely results from the fact that small islands (with $w/L \lesssim 0.02$) display a deficit of magnetic flux as compared to the expected value of $\Psi \sim B_0 w$, as shown in the third row of Fig. 5.

At larger sizes and fluxes ($w/L \gtrsim 0.01$ and $\Psi/B_0 L \gtrsim 0.01$), the distributions show a steeper decay, approximately as $N(w) \propto w^{-1}$ and $N(\Psi) \propto \Psi^{-1}$, which is consistent with the model of Uzdensky et al. (2010). The size distribution cuts off at $w/L \sim 0.2$, whereas the flux distribution terminates at $\Psi/B_0 L \sim 0.2$. We find that the reconnection layer might occasionally result in the formation of extraordinarily large plasmoids with $w/L \sim 0.3$–0.4, but their occurrence is extremely rare (not more than once every few tens of L/c). Overall, we conclude that the plasmoids routinely produced in the reconnection layer reach at most a width of $w^{\text{max}}/L \sim 0.2$.

This is in good agreement with the findings of non-relativistic MHD simulations, where the largest plasmoids (defined as 'monster plasmoids' by Uzdensky et al. 2010) reached a width of $\sim 0.2\,L$.[12]

We now proceed to describe the fourth, fifth and sixth rows in Fig. 5. They all illustrate the magnetic and kinetic energy content of plasmoids, as a function of size and magnetization. The comoving magnetic energy fraction in the fourth row of panels is computed as $\epsilon_B = \epsilon_{B,\,\text{lab}} - \epsilon_{E,\,\text{lab}}$, where the magnetic energy in the comoving frame is $B^2/8\pi = (B^2_{\text{lab}} - E^2_{\text{lab}})/8\pi$, assuming that the electric field vanishes in the plasmoid comoving frame. Alternatively, by defining $\epsilon_{\parallel,\text{lab}} = B^2_{x,\text{lab}}/8\pi n_0 mc^2$ and $\epsilon_{\perp,\text{lab}} = (B^2_{y,\text{lab}} + B^2_{z,\text{lab}})/8\pi n_0 mc^2$, the comoving magnetic energy fraction equals $\epsilon_B = \epsilon_{\parallel,\text{lab}} + \epsilon_{\perp,\text{lab}}/\Gamma^2$. We have verified that the two expressions yield nearly identical results. The comoving magnetic energy fraction scales in the large plasmoids as $\epsilon_B \sim \sigma$, as indicated by the dotted white lines and expected from pressure equilibrium. If the magnetic field in the plasmoids were to be the same as the field in the inflow, we would expect $\epsilon_B \sim \sigma/2$. It follows that the comoving magnetic field in the large plasmoids is on average $\sim\sqrt{2}\,B_0$. The apparent deficit in magnetic energy in the small plasmoids is directly related to the lack of magnetic flux discussed above, and it ultimately results from the decrease of magnetic field strength in the vicinity of the current sheet, as we describe in Appendix A. So, small plasmoids are still in pressure equilibrium with their surroundings, but the mean magnetic energy (both inside and outside the small plasmoids) is smaller than for larger plasmoids.

We have also measured the ratio of the 'parallel' and 'perpendicular' comoving magnetic energies, $\epsilon_{\parallel,\text{lab}}/(\epsilon_{\perp,\text{lab}}/\Gamma^2)$ (not shown in Fig. 5). We have verified that it is remarkably constant with respect to island size (in particular, it does not show the deficit at small islands of the overall magnetic energy fraction), and it is slightly larger than unity. This is in agreement with the fact that the plasmoids are nearly spherical, just slightly elongated along the direction parallel to the outflow (see the first row in Fig. 5).

The fifth row in Fig. 5 illustrates the internal energy content of secondary magnetic islands. The kinetic energy fraction in the plasmoid comoving frame ϵ_{kin} is computed from quantities measured in the simulation frame as

$$\epsilon_{\text{kin}} = \frac{\epsilon_{\text{kin,lab}} - (\Gamma - 1)n_{\text{lab}}/n_0}{\hat{\gamma}\Gamma^2 - (\hat{\gamma} - 1)}, \tag{4}$$

where we have assumed that the particle distribution in the plasmoid comoving frame is isotropic with adiabatic index $\hat{\gamma}$. The adiabatic index is computed iteratively using the Synge (1957)'s equation of state, and in all the cases, we find that $\hat{\gamma} \sim 4/3$. The assumption of an isotropic particle population is well realized in large plasmoids, as we demonstrate in Section 4.2.

In analogy to the magnetic energy fraction, the kinetic energy fraction scales as $\sim\sigma$, as indicated by the dotted white lines and expected from pressure equilibrium. For small islands, we notice the usual deficit, although it is much less dramatic for the kinetic energy fraction than for the magnetic energy fraction, for reasons that will be clarified in Appendix A. For large islands, the kinetic energy fraction is slightly larger than the magnetic energy fraction (compare the fourth and fifth rows in Fig. 5). This suggests that secondary plasmoids display a slight dominance of particle energy over magnetic energy.

---

[12] Note that in Loureiro et al. (2012), the overall system length was L, whereas it is $2L$ in our case. Also, they defined w to be the plasmoid half-width, whereas it is the full width in our work.

This is further illustrated in the sixth row of Fig. 5, which shows the equipartition parameter χ_{eq}. Following SPG15, this is defined as

$$\chi_{\text{eq}} = \frac{\int \frac{\varepsilon_{\text{kin}}}{\varepsilon_{\text{kin}}+\varepsilon_B}\varepsilon_{\text{kin}}\,dV}{\int \varepsilon_{\text{kin}}\,dV}, \tag{5}$$

where the integral is extended over the volume of the plasmoid, ε_{kin} is the particle kinetic energy density (as measured in the plasmoid rest frame) and ε_B is the comoving magnetic energy density. In the case of a proton–electron plasma, ε_{kin} should only include the kinetic energy of the radiating species, i.e. of the electrons. As appropriate for the fast cooling regime (see SPG15), the ratio $\varepsilon_{\text{kin}}/(\varepsilon_{\text{kin}} + \varepsilon_B)$ in equation (5) is weighted with the kinetic energy.

In the case of equipartition between kinetic and magnetic energy densities, we would expect $\chi_{\text{eq}} \sim 0.5$. The sixth row in Fig. 5 shows that, regardless of the magnetization or the plasmoid size, secondary islands are indeed close to equipartition, with only a slight dominance of the particle kinetic component, leading to $\chi_{\text{eq}} \sim 0.6$ (as indicated by the dotted white lines). This is consistent with the results in SPG15, where the equipartition parameter was measured by integrating over the entire plasmoid chain (rather than isolating individual plasmoids, as we are doing here). Finally, we remark that the tendency for $\chi_{\text{eq}} \to 1$ at small island sizes (most significantly for $\sigma = 3$, left-hand panel) is just related to the corresponding deficit of magnetic energy that we have discussed above, and that we explain in Appendix A.

We comment on the bottom-most panel in Fig. 5 in the next subsection, where we describe the particle spectrum and anisotropy in secondary plasmoids.

## 4.2 Particle spectrum and anisotropy in plasmoids

Fig. 7 describes the properties of the population of particles belonging to individual plasmoids, as a function of the plasmoid size and of the flow magnetization (with $\sigma = 3$ in the left-hand column, $\sigma = 10$ in the middle column and $\sigma = 50$ in the right-hand column).

In the top row, we plot the Larmor radius $r_{0i,\text{cut}} = p_{i,\text{cut}}c/eB_0$ of the positrons at the comoving cut-off momentum $p_{i,\text{cut}}$ along different directions ($i = x$ in green, $i = y$ in blue, $i = +z$ in solid red, $i = -z$ in dotted red) or the Larmor radius $r_{0,\text{cut}} = p_{\text{cut}}c/eB_0$ of the positrons at the total comoving cut-off momentum, regardless of the direction (black solid lines). The definition of the cut-off momentum is in equation (3), and the Larmor radius is normalized to the plasmoid width w. Each filled circle in the top row of Fig. 7 represents the mean value among the plasmoids whose width (as indicated on the horizontal axis, in units of L) falls in that range.

The Larmor radius $r_{0y,\text{cut}} = p_{y,\text{cut}}c/eB_0$ (blue lines) measured with the y component of the momentum transverse to the current sheet (which is Lorentz invariant) scales almost linearly with the plasmoid width w (equivalently, $r_{0y,\text{cut}}/w$ is a constant). This is also illustrated in the bottom-most row in Fig. 5, where we present the same ratio $r_{0y,\text{cut}}/w$ for all the plasmoids in our simulations, as a 2D histogram. Remarkably, the ratio $r_{0y,\text{cut}}/w$ is also nearly insensitive to the magnetization, and always around ~ 0.2 (as indicated by the dotted white lines in Fig. 5), with only a slight tendency for a lower value at $\sigma = 3$ (see the top-left panel in Fig. 7).

We argue that the ratio $r_{0y,\text{cut}}/w$ is an excellent indicator of the confinement capabilities of secondary plasmoids, i.e. of the highest energy particles that can stay trapped in a plasmoid of width w. In fact, the particles inflowing into the reconnection layer are initially accelerated by the reconnection electric field at the X-points (either the primary X-point or the series of secondary X-points in between
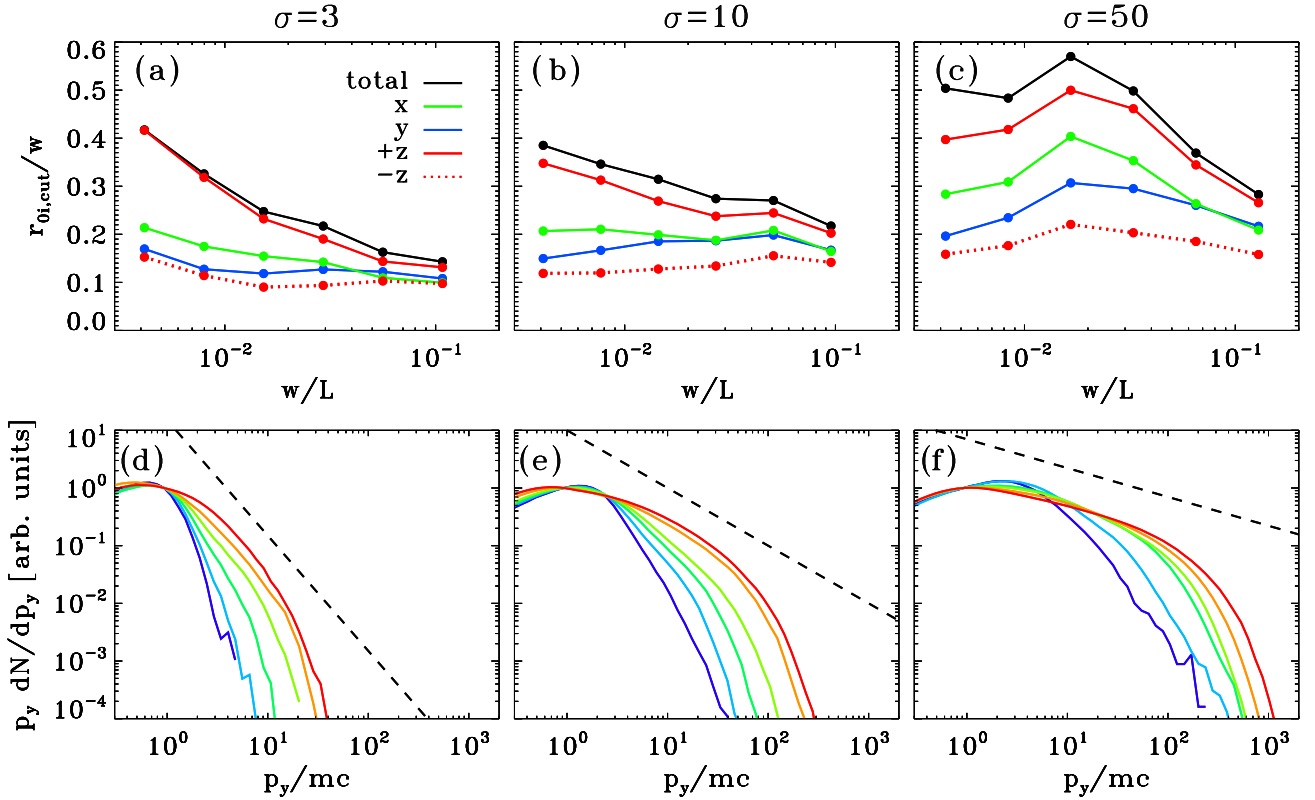
Figure 7. Spectrum and anisotropy as a function of the plasmoid width, for three values of the magnetization, as indicated at the top ($\sigma = 3$ in the left-hand column, $\sigma = 10$ in the middle column, and $\sigma = 50$ in the right-hand column). Top row: in bins of the plasmoid size w normalized to L, we plot the Larmor radius $r_{0i,\text{cut}} = p_{i,\text{cut}}c/eB_0$ of the positrons at the comoving cut-off momentum $p_{i,\text{cut}}$ ($i = x$ in green, $i = y$ in blue, $i = +z$ in solid red, $i = -z$ in dotted red) or the Larmor radius $r_{0,\text{cut}} = p_{\text{cut}}c/eB_0$ of the positrons at the total comoving cut-off momentum, regardless of the direction (black solid lines). Each data point represents the mean value among the plasmoids whose width falls in that range. While small plasmoids preserve a significant anisotropy in the direction of the accelerating electric field, large plasmoids have nearly isotropic particle distributions. Bottom row: momentum spectra of p_y, with the different colours corresponding to the six bins in width indicated in the top panels (from blue for small w, to red for large w). At large plasmoid widths, the spectrum approaches a power law, with slope $s \sim 3$ for $\sigma = 3$, $s \sim 2$ for $\sigma = 10$ and $s \sim 1.5$ for $\sigma = 50$, as indicated by the dashed lines.

secondary plasmoids), as described by Zenitani & Hoshino (2001) and SS14. At X-points, positrons are accelerated along the $+z$-direction and electrons in the opposite direction. Then, the tension force of the reconnected magnetic field advects the particles away from the X-point along the x-direction of the outflow, where they will be trapped in magnetic islands. So, before entering a magnetic island, the particle motion preferentially lies in the x–z plane. It follows that the outflowing particles can attain an appreciable component of momentum along the y-direction only by interaction with the toroidal magnetic loops of the islands. Larger islands will be able to scatter along y higher energy particles, and then to keep them confined within the island contour.

The value $r_{0y,\text{cut}}/w \sim 0.2$ can indeed be understood with a simple argument, based on particle confinement. A particle will stay trapped in a given plasmoid if its full Larmor circle is smaller than the island half-width (the B_x magnetic field switches sign on the two sides of the island, so the comparison is with the plasmoid half-width, rather than its full width). The most constraining condition will apply to the particles at the cut-off momentum $p_{y,\text{cut}}$, that need to have $2\,r_{0y,\text{cut}} \lesssim w/2$, or equivalently $r_{0y,\text{cut}}/w \lesssim 0.25$. This is remarkably close to the results shown by the blue lines in the top row of Fig. 7. The fact that the ratio $r_{0y,\text{cut}}/w$ is slightly smaller for $\sigma = 3$ than for higher magnetizations is probably due to our definition of $p_{i,\text{cut}}$ in equation (3), which overestimates the exponential cutoff of the momentum distribution by a factor of $n_{\text{cut}} - s$ (see

the discussion after equation 3). We always choose $n_{\text{cut}} = 6$, but the spectral slope s of the momentum distribution is a function of the magnetization (as we explain below), with $s \sim 3$ for $\sigma = 3$, $s \sim 2$ for $\sigma = 10$ and $s \sim 1.5$ for $\sigma = 50$. So, our definition of $p_{i,\text{cut}}$ overestimates the true cutoff momentum by a factor of ~ 3 for $\sigma = 3$ and ~ 4 to 5 for higher magnetizations. So, if we were to measure the Larmor radius with the true cut-off momentum, rather than our proxy in equation (3), we would obtain that it is a constant fraction of the plasmoid width, remarkably independent of the magnetization.

As shown by the top row in Fig. 7, the ratio $r_{0x,\text{cut}}/w$, with the cut-off momentum $p_{x,\text{cut}}$ measured in the plasmoid rest frame, follows closely the ratio $r_{0y,\text{cut}}/w$ for all the values of magnetization we explore. Thus, the ratio $r_{0x,\text{cut}}/w$ is also a good indicator of the confinement capabilities of secondary plasmoids. The fact that $r_{0x,\text{cut}}/w$ is slightly larger than $r_{0y,\text{cut}}/w$ for small islands (compare the green and blue lines in the top row of Fig. 7) is probably related to the fact that the plasmoid length is typically larger than its width by a factor of ~ 1.5 (see the top row in Fig. 5), so that particles with x momentum moderately higher than the y momentum can still stay confined in a plasmoid of given w.

While the positron cut-off momentum along the $-z$-direction follows the same trend as $p_{y,\text{cut}}$ and $p_{x,\text{cut}}$ (compare the dotted red line with the blue and green lines), the positron momentum along the $+z$-direction of the reconnection electric field shows a distinct

behaviour (solid red line in the top panels of Fig. 7). Small islands are highly anisotropic, with $p_{+z,\mathrm{cut}}$ appreciably larger than $p_{y,\mathrm{cut}}$ and $p_{x,\mathrm{cut}}$ (see also Cerutti et al. 2012, 2013; Kagan et al. 2016). As a small (and so, fast) island moves along the current sheet, it might stay in phase for a significant time with high-energy particles accelerated at a neighbouring X-point, that are now propagating along the current sheet. This results in a value of the positron cut-off momentum $p_{+z,\mathrm{cut}}$ (along the accelerating electric field) much larger than $p_{-z,\mathrm{cut}}$. For electrons, the opposite anisotropy is observed. The sign of the z anisotropy seen in the top row of Fig. 7 is consistent with the sign of the electric field at X-points, suggesting that direct acceleration by the reconnection electric field plays an important role in the early stages of particle acceleration Zenitani & Hoshino 2001; SS14; Nalewajko et al. 2015).[13] In contrast, the antireconnection electric field at the interface between merging islands is oriented along the $-z$-direction, and it would result in an anisotropy opposite to what is observed in Fig. 7. This suggests that the antireconnection electric field does not play a major role for the acceleration of the particles trapped in small islands. The fact that the z anisotropy in small islands is preferentially induced by the accelerating electric field at X-points is also revealed by the 2D pattern of the z anisotropy (not shown), whose strongest signal appears in the vicinity of the current sheet plane (i.e. for $|y| \ll w$).

Large islands are nearly isotropic, for all the magnetizations we have explored. As we demonstrate in Section 5, the transition between small anisotropic islands and large isotropic islands occurs at the same plasma scale, i.e. at a size that is a fixed multiple of $r_{0,\mathrm{hot}}$, for different values of the overall system length $L/r_{0,\mathrm{hot}}$. It follows that, for a realistic astrophysical system with $L/r_{0,\mathrm{hot}} \gg 1$, all but the smallest islands will be fairly isotropic. Kinetic simulations in small computational domains, due to the lack of a sufficient separation of scales between the plasma scales and the system size, might have artificially overemphasized the degree of particle anisotropy (Cerutti et al. 2012, 2013; Kagan et al. 2016), which is found to be quite low in the big islands of our large-scale simulations.

This also explains why, for a fixed w/L, the z anisotropy is more pronounced at higher magnetizations. As we have stated above, the degree of anisotropy depends primarily on $w/r_{0,\mathrm{hot}}$. Our domain size for $\sigma = 10$ is twice as big (in units of $r_{0,\mathrm{hot}}$) than for $\sigma = 50$. This explains why, at the same w/L, the case $\sigma = 50$ displays a higher degree of z anisotropy than the case $\sigma = 10$.

The residual weak anisotropy in large islands is not related to the reconnection electric field, but it is a consequence of the combined effect of the ∇B-drift and the curvature drift, both pointing along $+z$ for positrons (and in the opposite direction for electrons). As a result, the anisotropy is not localized in the vicinity of the $y = 0$ plane (as it is the case for small islands), but it is rather uniform over the plasmoid surface (not shown). For a relativistic particle, the magnitude of the drift speed scales proportionally to the ratio between the particle Larmor radius and the island half-width (which we take as a proxy for the scale length $\sim B/|\nabla B|$ or the curvature radius of field lines). This has two consequences. First, for a given island, the anisotropy in z will be maximal for the highest energy particles, since they will have a larger ratio of their Larmor radius to the island size. This trend is indeed observed (but not shown). Secondly, the black lines in the top panel of Fig. 7 show that the ratio of the Larmor radius at the total cut-off momentum (regardless of

direction) and the island size is a decreasing function of w. So, the drift speed at the total cut-off momentum will be larger for smaller islands, which explains the trend in anisotropy seen in Fig. 7 (but only at the high-w end, since we have argued that the anisotropy in small islands has a different origin).

The highest energy particles in the largest islands cannot be produced via direct acceleration by the reconnection electric field at X-points (Guo et al. 2014; SS14; Nalewajko et al. 2015). Werner et al. (2016) found that spectrum of particles produced at X-points should cut off at $\sim 4\sigma$ (see also fig. 5 in SS14). Given that our proxy for the cut-off momentum is a factor of a few larger than the true cutoff, it would correspond to a Larmor radius $r_{0,\mathrm{cut}} \sim 10\, r_{0,\mathrm{hot}}$, independently from the island size. In large islands, we argue that the high-energy cutoff of the particle spectrum is populated by particles accelerated during island mergers (Guo et al. 2014; SS14; Nalewajko et al. 2015). Let us assume that the accelerating electric field generated during island mergers is $\sim 0.2 B_0$, where we have taken the reconnection rate in between the two merging islands to be of the order of $\sim 0.15\, c$ and we have considered that the magnetic field in the plasmoids is a factor of ~ 1.5 larger than the field B_0 in the inflow (see the fourth row in Fig. 5). The potential energy available over a characteristic acceleration length of the order of $\sim w$ will be $\sim 0.2 e B_0 w$, which results in a Larmor radius $r_{0,\mathrm{cut}}/w \sim 0.2$. This simple argument shows that as a result of the merger of two large islands, particles can be accelerated so that to maintain the ratio $r_{0,\mathrm{cut}}/w$ close to 0.2, as required by our findings.

By equating $r_{0,\mathrm{cut}} \sim 10\, r_{0,\mathrm{hot}}$ (from X-point acceleration) with $r_{0,\mathrm{cut}}/w \sim 0.2$ (from acceleration in island mergers), we find a critical island size of $w/r_{0,\mathrm{hot}} \sim 50$. The highest energy particles in islands with $w/r_{0,\mathrm{hot}} \lesssim 50$ are primarily accelerated by the reconnection electric field at X-points (and we would expect a high degree of z anisotropy), whereas acceleration in island mergers dominates at $w/r_{0,\mathrm{hot}} \gtrsim 50$. In units of the system length L, we expect the transition to occur at $w/L \sim 0.07$ for $\sigma = 3$, at $w/L \sim 0.04$ for $\sigma = 10$ (for our fiducial case $L/r_{0,\mathrm{hot}} \simeq 1130$) and at $w/L \sim 0.1$ for $\sigma = 50$.

The bottom row in Fig. 7 shows how the momentum spectrum $p_y dN/dp_y$ of positrons trapped in plasmoids depends on the plasmoid size (different colours, from blue to red, correspond to the bins in width indicated by the filled circles in the top panels). As we demonstrate in Appendix B, most of the high-energy particles reside in plasmoids (more precisely, in the largest plasmoids), so the particle spectrum from plasmoids is an excellent proxy for the spectrum integrated over the whole current sheet (i.e. including the plasmoids as well as the regions in between islands).

The bottom row of Fig. 7 shows that the upper cutoff of the momentum spectrum scales linearly with the island size (the bins in width are logarithmically spaced), in agreement with the blue line in the top row. The spectral shape is a strong function of the island size. Small islands have a momentum distribution that is nearly thermal, since they cannot confine the highest energy particles accelerated at X-points. An extended power-law distribution appears in larger islands, since they can successfully trap all of the particles accelerated at X-points. The power-law slope in the largest islands is asymptoting to $s \sim 3$ for $\sigma = 3$, $s \sim 2$ for $\sigma = 10$ and $s \sim 1.5$ for $\sigma = 50$, as indicated by the dashed black lines in the three bottom panels. Such slopes are consistent with the values quoted in SS14, where the particle spectrum was integrated over the whole current sheet. As we demonstrate in Appendix B, most of the high-energy particles are contained within large islands. It follows that the spectrum measured in SS14, despite being integrated over the whole layer, was actually mostly contributed by the few largest islands. It

---

[13] The electric field at the ends of two coalescing islands (i.e. outside of the region in between the two islands) is also oriented along $+z$, but we do not expect small islands to have suffered many mergers.
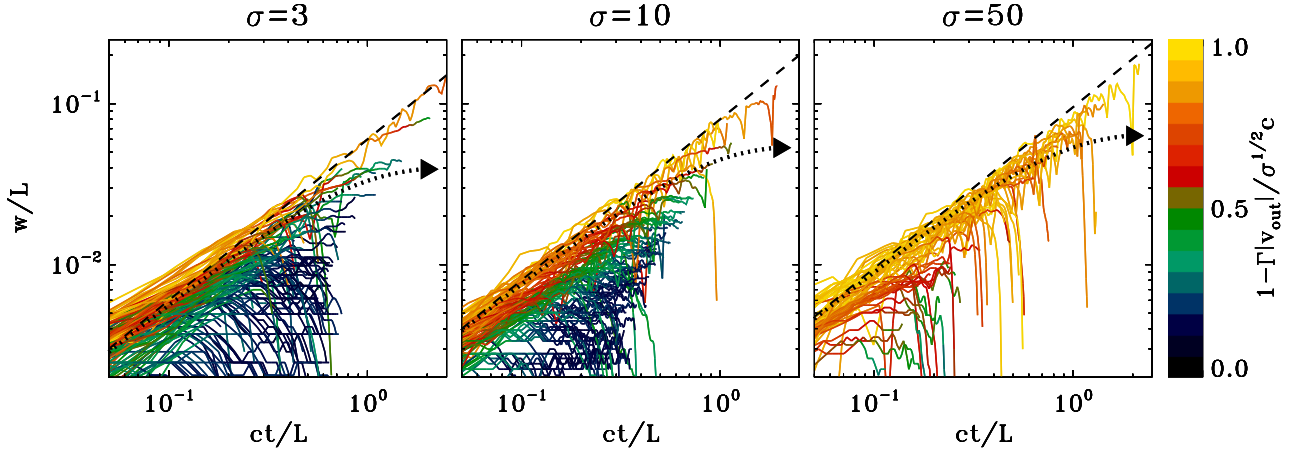
Figure 8. Growth of the plasmoid width as a function of the proper time, for three values of the magnetization, as indicated at the top ($\sigma = 3$ in the left-hand panel, $\sigma = 10$ in the middle panel, and $\sigma = 50$ in the right-hand panel). For the sake of clarity, we only plot the evolutionary tracks of plasmoids whose lifetime (in the lab frame) is longer than $\simeq 0.4L/c$. Colours indicate the plasmoid four-velocity, relative to the terminal four-velocity $\sim \sqrt{\sigma}\, c$ predicted by Lyubarsky (2005), as indicated by the colour bar (blue for fast plasmoids, yellow for slow plasmoids). It is apparent that most of the growth happens at slow velocities (yellow or red tracks), and that in this phase, the plasmoid width increases linearly with time (with a coefficient of $w/t \simeq 0.06\,c$ for $\sigma = 3$, $\simeq 0.08\,c$ for $\sigma = 10$ and $\simeq 0.1\,c$ for $\sigma = 50$, as indicated by the dashed black lines). When the plasmoid speed approaches the Alfvén speed (or equivalently, its four-velocity approaches $\sqrt{\sigma}\, c$), the plasmoid growth terminates, as schematically shown by the curved dotted lines with arrows.

is then quite natural to expect that the spectral slope of the largest islands in Fig. 7 is comparable to the power-law index found in SS14, for all the magnetizations we explore.

In the regime $\sigma \gg 1$, one expects that the mean energy per particle in the plasmoids should scale as $\propto \sqrt{\sigma}$ (Lyubarsky 2005). Since small islands have nearly-thermal particle spectra, one would expect the same scaling for the peak momentum, as long as it exceeds unity. In fact, the peak of the blue curve in panel (e) lies at $p_y/mc \sim 1.5$, whereas it is close to $p_y/mc \sim 3$ for the blue line in panel (f). This is consistent with the predicted scaling $\propto \sqrt{\sigma}$.[14] For a given magnetization, the mean energy per particle should be independent of the plasmoid size, which explains why for larger sizes, as the particle spectrum extends to higher momenta, the low-energy cutoff also recedes to lower values. This is more pronounced for $\sigma = 10$ and 50 than for $\sigma = 3$, since the power-law slope for $\sigma = 3$ is so steep that most of the energy content is controlled by the particles at the low-energy cutoff, which is then expected to stay nearly the same as we vary the plasmoid width.

In the bottom row of Fig. 7, we have chosen to display the momentum spectrum along the direction transverse to the current sheet to emphasize the confinement capabilities of plasmoids of different sizes. We find that the comoving momentum spectrum $p_x\mathrm{d}N/\mathrm{d}p_x$ is nearly identical (not shown; yet, compare the blue and green lines in the top row), and also similar to $[p_z\mathrm{d}N/\mathrm{d}p_z]_{p_z<0}$, i.e. the z momentum spectrum of positrons having $p_z < 0$ (or similarly, of electrons having $p_z > 0$). In contrast, the spectrum $[p_z\mathrm{d}N/\mathrm{d}p_z]_{p_z>0}$ of positrons having $p_z > 0$ shows a harder spectral slope (even for relatively small islands), resulting from particles accelerated by the reconnection electric field at X-points (see Appendix B).

4.3 Plasmoid growth

By following individual plasmoids over time, we can quantify the rate at which they grow. This is illustrated in Fig. 8, where we present

the temporal evolution of the plasmoid width (time is measured in the plasmoid rest frame), for three values of the magnetization, as indicated at the top ($\sigma = 3$ in the left-hand panel, $\sigma = 10$ in the middle panel, and $\sigma = 50$ in the right-hand panel). For the sake of clarity, we only plot the evolutionary tracks of plasmoids whose lifetime (in the lab frame) is longer than $\simeq 0.4L/c$.

We find that in the plasmoid rest frame, the growth in plasmoid width proceeds at a constant rate

$$\frac{\mathrm{d}w}{c\,\mathrm{d}t} = \beta_\mathrm{g}, \tag{6}$$

where the coefficient β_g has a weak dependence on magnetization. As indicated by the three dashed black lines in Fig. 8, $\beta_\mathrm{g} \simeq 0.06$ for $\sigma = 3$, $\beta_\mathrm{g} \simeq 0.08$ for $\sigma = 10$ and $\beta_\mathrm{g} \simeq 0.1$ for $\sigma = 50$. For all the values of σ, we find that β_g is about half of the reconnection inflow rate $|v_\mathrm{in}|/c$ (see the top panel in Fig. 3). We have also verified that our results are not consistent with the assumption of constant growth in the laboratory frame. Rather, since it is in the plasmoid rest frame that the growth rate is constant, the increase in plasmoid width in the simulation frame follows $\mathrm{d}w/c\,\mathrm{d}t_\mathrm{lab} = \beta_\mathrm{g}/\Gamma$, where Γ is the plasmoid bulk Lorentz factor. In Section 4.3.1, we propose a toy model to corroborate our results.

The colored tracks in Fig. 8 confirm that the growth of the largest plasmoids proceeds at a constant rate in the comoving frame, following the black dashed lines. The sudden dips that occasionally appear in the tracks (e.g. at $ct/L \sim 2$ in the right-hand panel) are a consequence of the apparent shrinking in the plasmoid size that accompanies island mergers (see the beginning of Section 4 in relation to Fig. 4). Soon after the merger, the surviving plasmoid (defined as the larger of the two that merged) recovers its proper width. The smaller of the two merging plasmoids terminates its life trajectory. This explains why in Fig. 8 smaller plasmoids tend to have shorter lives, since they are more likely to encounter a larger plasmoid that swallows them.

The colour coding in Fig. 8 indicates the plasmoid four-velocity, relative to the expected terminal four-velocity $\sim \sqrt{\sigma}\, c$ (more precisely, colours indicate $1 - \Gamma|v_\mathrm{out}|/\sqrt{\sigma}\, c$). Most of the plasmoid growth happens while the islands are still non-relativistic (yellow

---

[14] For $\sigma = 3$, the peak is at even lower values, but since it lies at non-relativistic speeds, we would not necessarily expect that it scales as $\propto \sqrt{\sigma}$.

in Fig. 8). When the plasmoids approach the Alfvén speed (so, their four-velocity becomes closer to $\sim\sqrt{\sigma}\,c$), the accretion rate diminishes and the plasmoid width saturates (green and blue in Fig. 8). As a result, their tracks deviate from the locus of constant growth indicated by the dashed black lines in Fig. 8 (as sketched by the curved dotted lines with arrows in Fig. 8). For example, the two plasmoids that live longest in the middle panel (for $\sigma = 10$) deviate from the $\mathrm{d}w/c\,\mathrm{d}t = 0.08$ curve when their four-velocity reaches $\sim 0.5\sqrt{\sigma}\,c$, and after this point, their width stays nearly unchanged.

For each plasmoid, we have tracked the trajectories of the particles that get trapped within the plasmoid, which allows us to clarify how the plasmoid growth proceeds. We find that most of the long-lasting plasmoids are born close to the centre of the current sheet. The longer they spend in the vicinity of $x \sim 0$ in their early life (see the position-time tracks in Fig. 4), the larger they will eventually become. While they stay in the vicinity of the centre (roughly speaking, within a distance of a few times their size), the islands accrete from both sides of the current sheet. Eventually, the tension force of the field lines pulls them away from the centre. At a given distance from the current sheet, the speed of a plasmoid is inversely proportional to its size, as we show in Section 4.4. It follows that while its speed is still non-relativistic, a given plasmoid mostly accretes smaller (so, faster) plasmoids that are trailing in its wake. As it accelerates to relativistic speeds, the accretion rate from the trailing side decreases, since now the plasmoid is moving at the same speed ($\sim c$) as all of the smaller plasmoids in its wake, and the trailing islands cannot catch up with it. At this point, most of the accreted particles come from the region ahead of the plasmoid.

Fig. 9 shows that accretion of particles in the current sheet can lead to the formation of 'monster plasmoids' whose width reaches $w/L \sim 0.2$, in agreement with the findings of MHD simulations of non-relativistic reconnection (Loureiro et al. 2012). Fig. 9 refers to a system with $\sigma = 10$ and $L/r_{0,\mathrm{hot}} \simeq 127$, but we have verified that this conclusion holds regardless of σ or $L/r_{0,\mathrm{hot}}$. Extraordinarily large plasmoids with $w/L \sim 0.3$–0.4 might be occasionally produced, but their occurrence is extremely rare (not more than once every few tens of L/c). In fact, in the timespan of $\sim 14\,L/c$ covered by Fig. 9, no plasmoid larger than $\sim 0.2\,L$ is produced.

The red curve in the top panel of Fig. 9 shows the width of the largest plasmoid existing in our domain as a function of time. The other curves show the width of the second largest plasmoid (in yellow) down to the fifth largest plasmoid (in black), showing that plasmoids with $w/L \sim 0.05$ occur much more frequently than the monster plasmoid with $w/L \sim 0.2$ (as we have already described in Fig. 6). The largest plasmoid (red curve in the top panel of Fig. 9) grows at a fraction ~ 0.1 of the speed of light, in agreement with the conclusions of Fig. 8. This can be measured from the temporal slope of the red curve in the top panel: in the time interval $1 \lesssim ct_{\mathrm{lab}}/L \lesssim 3$, the plasmoid width increases up to $0.2\,L$, as indeed expected for a growth rate of $\sim 0.1\,c$.[15] The sudden drop in the red curve at $ct_{\mathrm{lab}}/L \sim 3.5$ occurs when the large plasmoid is ejected from the current sheet. At this point, the plasmoid that used to be the second largest (see the yellow curve in the top panel at $ct_{\mathrm{lab}}/L \sim 3.5$) becomes the largest one in the domain (and the third largest becomes the second largest, and so on).

The red curve in the top panel of Fig. 9 demonstrates that the typical recurrence time of monster plasmoids is $\sim 2.5\,L/c$ (see the
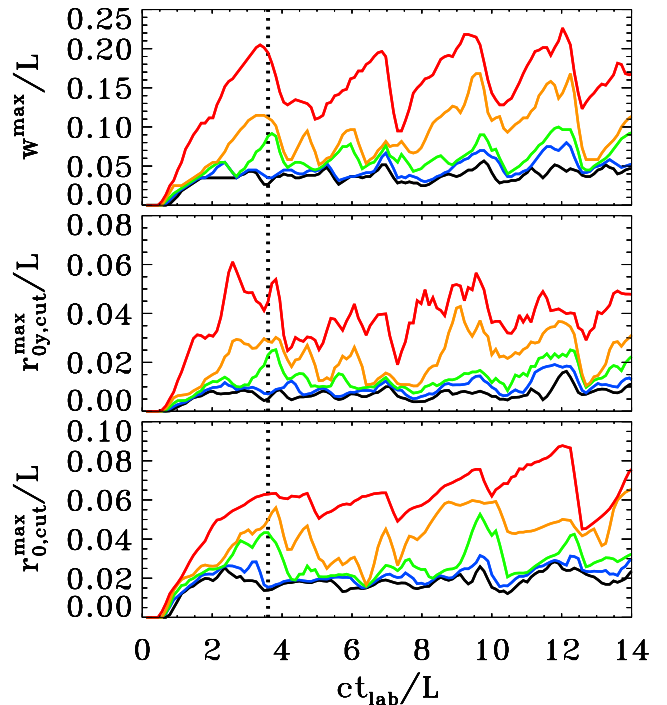
Figure 9. Temporal evolution of the properties of the five largest plasmoids (from the largest in red to the fifth largest in black), as a function of time in the laboratory frame, for a simulation with $\sigma = 10$ and $L \simeq 127\,r_{0,\mathrm{hot}}$. Top panel: width of the five largest plasmoids, in units of the system size L. Middle panel: the five plasmoids with the largest value of the positron Larmor radius $r_{0y,\mathrm{cut}} = p_{y,\mathrm{cut}}c/eB_0$, where $p_{y,\mathrm{cut}}$ is the cut-off momentum in the y-direction. Bottom panel: same as in the middle panel, but for the total comoving positron momentum, rather than its y component. The dotted black line shows the characteristic timespan ($\sim 3.6\,L/c$) of our fiducial runs. The panels show that the typical recurrence time for the largest plasmoids (having a width $w^{\mathrm{max}} \sim 0.2\,L$) is $\sim 2.5\,L/c$, and that the temporal evolutions of $r_{0y,\mathrm{cut}}^{\mathrm{max}}$ and $r_{0,\mathrm{cut}}^{\mathrm{max}}$ closely follow the time track of w^{max}.

quasi-periodic peaks in the red curve).[16] This is indeed the time needed to grow a plasmoid up to the monster width of $w/L \sim 0.2$, since the growth proceeds at a rate $\sim 0.08\,c$ (see the middle panel in Fig. 8). In turn, this implies that most of the plasma flowing into the current sheet within this time interval is accreted on to the monster plasmoid that is currently present in the reconnection layer. It is only when the monster plasmoid is ejected from the current sheet that another plasmoid can grow to monster-like sizes.

The middle panel in Fig. 9 presents the five plasmoids with the five largest values (from red to black) of the positron Larmor radius $r_{0y,\mathrm{cut}} = p_{y,\mathrm{cut}}c/eB_0$, where $p_{y,\mathrm{cut}}$ is the cut-off momentum in the y-direction. The temporal evolution of the curves in the middle panel displays a remarkable correlation with the lines in the top panel (compare curves of the same colour). This is in agreement with the results shown in Fig. 5 (bottom-most row) and in Fig. 7 (top row), i.e. the Larmor radius computed with the cut-off momentum $p_{y,\mathrm{cut}}$ scales linearly with the island size. Those two plots showed that this linear relation holds for all sizes, whereas Fig. 9 only focuses on the largest plasmoids, with size $w/L \gtrsim 0.05$. From the top and

---

[15] As we demonstrate in Section 4.4, large plasmoids move at non-relativistic speeds, so no relativistic corrections are required to transform from the comoving to the laboratory time.

[16] It follows that the simulation timespan of $\sim 3.6\,L/c$ of our fiducial runs (indicated with a vertical dotted black line in Fig. 9) is sufficient to capture the steady state physics of the system, and in particular the occurrence of monster plasmoids.

middle panels in Fig. 9, one can compute that the coefficient of the linear scaling is around $r_{0y,\text{cut}}/w \sim 0.2$, in excellent agreement with Fig. 5 and Fig. 7.

The top row in Fig. 7 showed that the largest plasmoids are nearly isotropic, and the upper cutoff in their momentum spectrum (black lines; regardless of the direction) is comparable to the cutoff momentum in the y-direction (blue lines). This is confirmed by the bottom panel in Fig. 9, where the curves display the plasmoids with the five largest values (from red to black) of the total positron Larmor radius $r_{0,\text{cut}} = p_{\text{cut}}c/eB_0$. The evolution of the curves in the bottom panel is well correlated in time with the lines in the middle panel (compare curves of the same colour), and their ratio is of the order of unity, i.e. $r_{0,\text{cut}} \gtrsim r_{0y,\text{cut}}$, in agreement with the top row in Fig. 7 at the largest sizes ($w/L \gtrsim 0.05$).

4.3.1 Toy model for the plasmoid growth

We now present a toy model for the plasmoid growth, in support of the numerical findings presented above. Let us assume that each plasmoid of size w is accreting material from a 'distance of influence' d_w, as measured along the current sheet in the plasmoid rest frame. An empirical estimate of the distance of influence will be given below. This implies that the number of particles N_{prt} in the plasmoid will grow, in the comoving frame, as

$$\frac{dN_{\text{prt}}}{c\,dt} = 2n_0 \frac{|v_{\text{in}}|}{c} d_w, \tag{7}$$

where the factor of 2 accounts for accretion from the two sides of the current sheet (the flux of particles perpendicular to the current sheet is Lorentz invariant). The plasmoid area is $\sim \pi w w_\parallel/4 \simeq w^2$, where we have used that $w_\parallel \simeq 1.5\,w$ (see the top row in Fig. 5). If n is the plasmoid mean density, the number of particles in the plasmoid will be $N_{\text{prt}} \simeq nw^2$. This implies that the plasmoid width increases at a rate

$$\frac{dw}{c\,dt} \simeq \frac{n_0}{n} \frac{|v_{\text{in}}|}{c} \frac{d_w}{w}, \tag{8}$$

where we have assumed that the comoving density n does not significantly change with time. To estimate the distance of influence d_w, one can assume that all the plasma that is attracted to a given island will eventually accrete on to that island. The electric current integrated over the surface of an island of size w is proportional to w, so its distance of influence will also scale linearly with w. By following the trajectories of the particles that will eventually accrete on to a given plasmoid, we can measure the distance of influence in our simulations, and we find that it is of the order $d_w \sim 2\,w$ for all the magnetizations we explore. Since $n/n_0 \sim 3$–5 regardless of σ (second row in Fig. 5), we find that the plasmoid size grows as

$$\frac{dw}{c\,dt} \simeq 0.5 \frac{|v_{\text{in}}|}{c}, \tag{9}$$

which is consistent with our numerical findings.

4.4 Plasmoid acceleration

After growing by accretion, secondary plasmoids are accelerated by the tension force of the reconnected magnetic field up to ultra-relativistic speeds, while they propagate towards the boundaries of the domain ('first they grow, then they go'). We find that, at a given distance from the centre of the current sheet, larger plasmoids tend to be slower. We find that the shape of the bulk acceleration profile becomes universal (i.e. the same for all the plasmoids in a given system) if the plasmoid four-velocity Γv_{out} along the outflow

direction is measured as a function of the distance $x - x_0$ from their birth location x_0, normalized to the instantaneous plasmoid width w. This is demonstrated in Fig. 10, which shows that, once the distance along the current sheet is in units of the plasmoid width w, all the plasmoid tracks overlap, regardless of the plasmoid size (which is indicated by the colours, see the colour bar on the right).

We find a universal profile of the form (see the dashed pink lines in Fig. 10)

$$\Gamma \frac{v_{\text{out}}}{c} \simeq \sqrt{\sigma} \tanh\left(\frac{\beta_{\text{acc}}}{\sqrt{\sigma}} \frac{x - x_0}{w} \right), \tag{10}$$

where x_0 is the plasmoid location at its birth, and the dimensionless acceleration rate $\beta_{\text{acc}} \simeq 0.12$ is nearly independent of the flow magnetization (with only a minimal tendency to increase for higher reconnection rates, i.e. higher σ). For $\sigma = 10$, we have also verified that the acceleration rate β_{acc} does not depend on the overall system length $L/r_{0,\text{hot}}$, from $L/r_{0,\text{hot}} \simeq 127$ up to $L/r_{0,\text{hot}} \simeq 1130$.

Equation (10) implies that high velocities (or equivalently, for $\beta_{\text{acc}}|x - x_0| \gtrsim \sqrt{\sigma}w$, the plasmoids approach the terminal four-velocity $\sim \sqrt{\sigma}\,c$. On the other hand, at low velocities (or equivalently, for $\beta_{\text{acc}}|x - x_0| \lesssim \sqrt{\sigma}w$), the scaling is

$$\Gamma \frac{v_{\text{out}}}{c} \sim \beta_{\text{acc}} \frac{x - x_0}{w}. \tag{11}$$

This implies that: (i) monster plasmoids with $w/L \sim 0.2$ leave the system at trans-relativistic speeds, with $|v_{\text{out}}|/c \sim 0.5$; (ii) the largest plasmoids capable of reaching the end of the current sheet (i.e. $|x| \sim L$) with the terminal four-velocity $\sim \sqrt{\sigma}\,c$ have a final width of $w/L \sim \beta_{\text{acc}}/\sqrt{\sigma} \sim 0.1/\sqrt{\sigma}$, i.e. they are systematically smaller at higher magnetizations.

The scaling in equation (11) has a simple empirical justification. Quite generally, we can equate the growth time up to a width w, which equals $t_{\text{g, lab}} \sim \Gamma w/\beta_{\text{g}}$ in the lab frame, with the acceleration/propagation time up to a distance $x - x_0$ from the plasmoid birth place, which is $t_{\text{acc, lab}} \sim c(x - x_0)/v_{\text{out}}$, finding that

$$\Gamma \frac{v_{\text{out}}}{c} \sim \beta_{\text{g}} \frac{x - x_0}{w}. \tag{12}$$

This has the same form as equation (11), and by comparison, we argue that $\beta_{\text{acc}} \sim \beta_{\text{g}} \sim 0.1$, as indeed we find in our simulations.

The right-hand panel in Fig. 10 shows that for $\sigma = 50$, only few islands can approach the terminal dimensionless four-velocity $\sim \sqrt{\sigma} \sim 7$, as compared to the copious number of fast plasmoids observed for $\sigma = 3$ and 10. Yet, since regions with four-velocity as fast as $\sim \sqrt{\sigma}\,c \sim 7\,c$ are present in the reconnection layer, in the fast smooth outflows in between magnetic islands (see the red line in the bottom panel of Fig. 3), we anticipate that, for a sufficiently large system, a number of plasmoids will be capable of reaching the expected terminal four-velocity $\sim \sqrt{\sigma}\,c$, even for $\sigma = 50$.

The apparent lack of fast plasmoids for $\sigma = 50$ is due to three main reasons. First, for a given final plasmoid size w (in units of $r_{0,\text{hot}}$), acceleration to the terminal speed requires a length $L/r_{0,\text{hot}} \gtrsim \sqrt{\sigma}\beta_{\text{acc}}^{-1}(w/r_{0,\text{hot}})$, i.e. larger domains (i.e. larger $L/r_{0,\text{hot}}$) are needed at higher σ. For comparison, our domain length for $\sigma = 10$ is $L/r_{0,\text{hot}} \simeq 1130$, which implies that we should use $L/r_{0,\text{hot}} \sim 2500$ for $\sigma = 50$, in order to capture a sufficient number of plasmoids moving at the terminal speed (rather, our domain for $\sigma = 50$ is $L/r_{0,\text{hot}} = 505$). Secondly, as we have described above, the critical size of the largest plasmoid that can reach the terminal Alfvén velocity is $\sim 0.1\,L/\sqrt{\sigma}$, so it is smaller at higher σ. This implies that the probability for such a plasmoid to accrete on to a larger and slower plasmoid is higher at stronger magnetizations (since the 'target' plasmoid can range in size from the monster width of $\sim 0.2\,L$
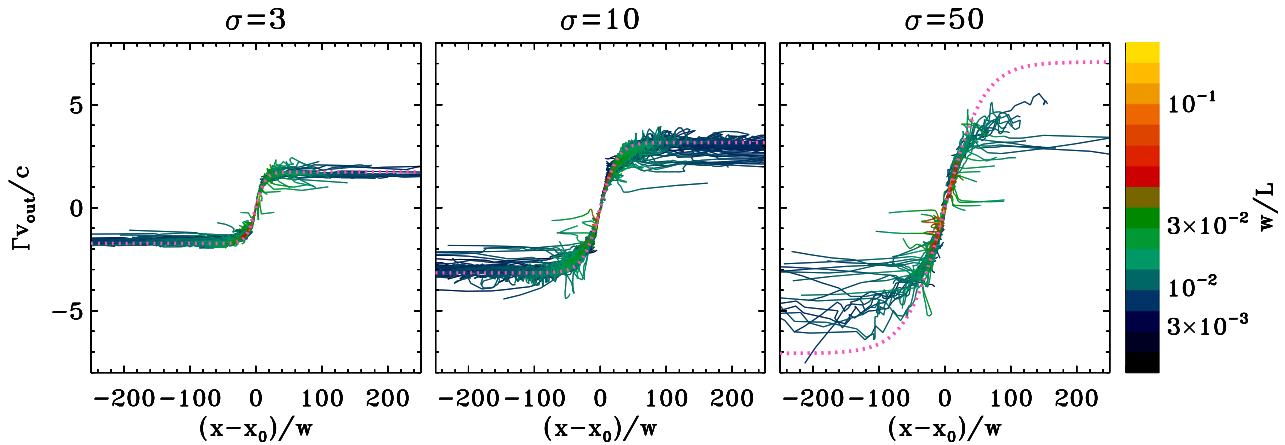
Figure 10. Plasmoid four-velocity along the outflow direction as a function of distance $(x - x_0)$ from their birth location x_0, normalized to the instantaneous plasmoid width w, for three values of the magnetization, as indicated at the top ($\sigma = 3$ in the left-hand panel, $\sigma = 10$ in the middle panel, and $\sigma = 50$ in the right-hand panel). For the sake of clarity, we only plot the tracks of plasmoids whose lifetime (in the lab frame) is longer than $\simeq 0.35 L/c$. Once the distance along the current sheet is normalized with the plasmoid width w, we show that all the tracks overlap, regardless of the plasmoid size (which is indicated by the colours, see the colour bar on the right). The plasmoid four-velocity follows a universal profile $\Gamma v_{\mathrm{out}}/c \simeq \sqrt{\sigma} \tanh[0.12(x - x_0)/\sqrt{\sigma} w]$, where the coefficient of $\simeq 0.12$ is nearly insensitive to the magnetization (see the pink dotted lines in the three panels, for the three values of σ).

down to the width of the 'projectile' plasmoid $\sim 0.1 L/\sqrt{\sigma}$). The small and fast plasmoid disappears into the large and slow one that lies ahead, before reaching the terminal four-velocity. The third reason is the fact that interactions among the plasmoids are stronger at higher magnetizations, as we have discussed at the beginning of Section 4. As a result, a small and fast plasmoid that is formed ahead of a large and slow one gets pulled back, inhibiting its acceleration. For the second and third reasons, we still expect that the number of plasmoids capable of reaching the expected terminal four-velocity $\sim \sqrt{\sigma} c$ will be smaller for $\sigma = 50$ than for lower magnetizations, even at the same value of $L/\sqrt{\sigma} r_{0,\mathrm{hot}}$.

We have explicitly verified that it is the tension of the field lines that is responsible for the plasmoid bulk acceleration. Since the total magnetic and kinetic energy content of a plasmoid with width w scales as $\propto \sigma w^2$ in the plasmoid comoving frame, its momentum in the lab frame will be $\propto \sigma w^2 \Gamma v_{\mathrm{out}}$. From equations (6) and (11), it follows that the force exerted on the plasmoid in the simulation frame (i.e. the time derivative of its momentum in the lab frame) scales as $\propto \sigma w v_{\mathrm{out}}/c$, until the plasmoid reaches the terminal four-velocity. By measuring the tension force exerted on each plasmoid by the bundle of field lines lying between the plasmoid contour and its trailing X-point, we have successfully assessed that it is indeed the magnetic field tension that drives the plasmoid bulk acceleration.

We now present a toy model to support why the magnetic tension force should scale as $\propto w v_{\mathrm{out}}/c$, or equivalently (using equation 11), as $\propto w \min[1, \beta_{\mathrm{acc}} x/w]$, assuming for the sake of simplicity that the plasmoid starts at $x_0 \sim 0$. For a plasmoid sufficiently far from the centre, the accelerating force will be provided by a cone of field lines trailing behind the plasmoid. The opening angle of the cone is $\sim |v_{\mathrm{in}}|/c$ (as predicted by Lyubarsky (2005), this is the inclination angle of the field lines) and its apex lies at a distance $d_{\mathrm{apex}} \sim (c/|v_{\mathrm{in}}|) w/2$ behind the plasmoid. For a plasmoid sufficiently far from the centre, all of the field lines between the apex and the plasmoid will contribute to provide the accelerating force, which would then scale as $\propto w$. In contrast, if the apex lies beyond the centre of the current sheet (i.e. to the other side, as compared to the plasmoid location), only a fraction of the field lines would be available for acceleration (in the special case of a plasmoid that lies

close to the centre, the tension force is expected to vanish). This happens when the plasmoid distance from the centre is $x \lesssim d_{\mathrm{apex}}$, in which case, only a fraction $\sim x/d_{\mathrm{apex}}$ of the field lines will be employed for acceleration. Putting everything together, the tension force should scale as $\propto \min[x, d_{\mathrm{apex}}] \propto w \min[1, 2(|v_{\mathrm{in}}|/c) x/w]$, in good agreement with our numerical results.

5 DEPENDENCE ON THE SYSTEM LENGTH

In this section, we describe how our results depend on the overall length of the system L, measured in units of the Larmor radius $r_{0,\mathrm{hot}} = \sqrt{\sigma} c/\omega_{\mathrm{p}}$ of the particles heated/accelerated by reconnection.[17] We focus on our fiducial magnetization $\sigma = 10$ and we vary the system length $L/r_{0,\mathrm{hot}}$ from 127 up to 1130. In all the cases, the simulation timespan is $\sim 3.6 L/c$, for fair comparison among the different values of $L/r_{0,\mathrm{hot}}$.

We find that both the plasmoid growth rate β_{g} and the acceleration rate β_{acc} are nearly identical over the range of $L/r_{0,\mathrm{hot}}$ that we explore. The plasmoid fluid properties presented in Fig. 5 do not depend on the overall system length. As we have anticipated in Section 4.1, the value of w/L where the lack of magnetic flux starts to appear (i.e. smaller islands have a deficit of magnetic flux, as compared to the scaling $\Psi/B_0 w \sim 1$ realized at larger widths) is always $w/L \sim 0.02$ regardless of the system length.

Fig. 11 quantifies how the size of the largest plasmoids and the maximum energy of accelerated particles depend on the system length L. In the top panel, the red line shows the plasmoid that, in the course of its history, reaches the largest width; the yellow line shows the second largest, and so on until the fifth largest plasmoid (black line). The width of the largest plasmoid (red curve) is affected by the limited timespan of our simulations. In fact, Fig. 9 shows, for the case $L/r_{0,\mathrm{hot}} \simeq 127$, that a timespan of $\sim 3.6 L/c$ (as indicated by the dotted vertical black line in Fig. 9) is barely sufficient to capture the full growth of the largest plasmoid. From the second

---

[17] We remind that the overall extent of our simulation domain in the x-direction of the outflow is actually $2L$.
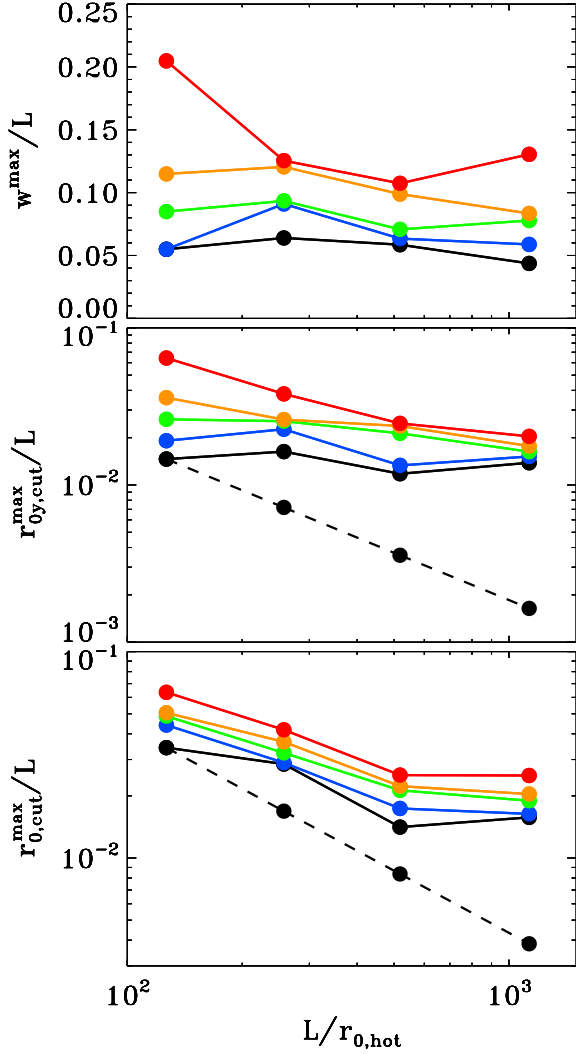
Figure 11. Scalings of plasmoid properties with respect to the overall system length L, as measured in units of $r_{0,\text{hot}}$, from $L/r_{0,\text{hot}} \simeq 127$ up to $L/r_{0,\text{hot}} \simeq 1130$. In all the cases, the simulation timespan is $\sim 3.6\,L/c$. Top panel: the red line shows the plasmoid that, in the course of its history, reaches the largest width; the yellow line shows the second largest, and so on until the fifth largest plasmoid (black line). The width of the few largest plasmoids approaches a fixed fraction of the system size L, which is independent of the length L itself. Middle panel: the red line shows the plasmoid that, in the course of its history, reaches the largest value of the positron Larmor radius $r_{0y,\text{cut}} = p_{y,\text{cut}}c/eB_0$, where $p_{y,\text{cut}}$ is the cut-off momentum in the y-direction. Similarly, the yellow line shows the plasmoid that reaches the second largest value, and so on until the fifth largest value (black line). At large L, the maximum Larmor radius approaches a fixed fraction of the overall system length L, independently of L. For comparison, the dashed black line shows the scaling $r_{0y,\text{cut}}^{\max}/L \propto L^{-1}$ expected if the maximum cut-off $p_{y,\text{cut}}^{\max}$ were to saturate. Bottom panel: same as in the middle panel, but for the total comoving positron momentum, rather than its y component. This can be regarded as the Hillas criterion for relativistic reconnection.

to the fifth largest plasmoids (yellow to black lines in Fig. 11), we are not affected by the limited timespan of our simulations, since the number of plasmoids increases at smaller widths. The corresponding curves in the top panel of Fig. 11 show that the width of the few largest plasmoids is a fixed fraction of the system length L, irrespective of $L/r_{0,\text{hot}}$.

We find that the linear scaling between plasmoid width w and Larmor radius $r_{0y,\text{cut}}$ of the particles at the cut-off y momentum holds regardless of the system length. Since the largest plasmoids have $w/L \sim 0.05$–0.2 independently of the system length (top panel), it is then not surprising that the largest values of the positron Larmor radius $r_{0y,\text{cut}}$ scale linearly with the system size, as shown in the middle panel of Fig. 11. The normalization of the curves in the middle panel is consistent with the relation $r_{0y,\text{cut}}/w \sim 0.2$ discussed in Section 4.2 and with the ratios w/L presented in the top panel (in fact, the slight decay of the red curve in the middle panel is to be correlated with the red line in the top panel). This suggests that the maximum y momentum of particles accelerated in reconnection scales linearly with the system size L. In contrast, if reconnection were to give a maximal value of the positron y momentum that stays constant with L, we would expect that $r_{0y,\text{cut}}^{\max}/L \propto L^{-1}$ in the middle panel of Fig. 11. This is shown as a dashed black line, and it is clearly inconsistent with our data.

These conclusions are further supported by the bottom panel in Fig. 11. There, we perform a similar analysis as in the middle panel, but for the total comoving positron momentum, rather than its y component. All the curves (from red for the largest value of the Larmor radius $r_{0,\text{cut}}$, down to black for the fifth largest) display a similar trend, decreasing as $r_{0,\text{cut}}^{\max}/L \propto L^{-1}$ for $L/r_{0,\text{hot}} \lesssim 300$ (compare with the dashed black line), and flattening out for $L/r_{0,\text{hot}} \gtrsim 300$. We attribute the transition to a change in the dominant mechanism for particle acceleration. At relatively small system sizes, particle acceleration by the reconnection electric field at X-points dominates (e.g. Zenitani & Hoshino 2001). The accelerated positrons move preferentially along the $+z$-direction of the electric field (and electrons in the opposite direction). The particle distribution is highly anisotropic, and the total momentum is primarily controlled by its z component (see the top row in Fig. 7). This explains why the decreasing trend in the bottom panel of Fig. 11, which is driven by the z momentum, does not appear in the middle panel, where the Larmor radius $r_{0y,\text{cut}}$ is computed using the y momentum. At this stage (i.e. for $L/r_{0,\text{hot}} \lesssim 300$), the maximum energy of accelerated particles is controlled by the acceleration capabilities of X-points. As anticipated in Section 4.2, the upper cutoff in the momentum spectrum of particles accelerated at X-points corresponds to a Larmor radius $r_{0,\text{cut}} \sim 10\,r_{0,\text{hot}}$, regardless of the system length L. This explains why for $L/r_{0,\text{hot}} \lesssim 300$ the Larmor radius of the highest energy particles scales as $r_{0,\text{cut}}^{\max}/L \propto L^{-1}$. This is in agreement with the results by Werner et al. (2016).

For larger systems (i.e. at $L/r_{0,\text{hot}} \gtrsim 300$), particle acceleration during island mergers plays a more and more dominant role. The potential energy available during the merger of two islands of width $\sim w$ is $\sim 0.2 eB_0 w$,[18] which results in a Larmor radius $r_{0,\text{cut}} \sim 0.2\,w$. By equating $r_{0,\text{cut}} \sim 10\,r_{0,\text{hot}}$ (from X-point acceleration) with $r_{0,\text{cut}} \sim 0.2\,w$ (from acceleration in mergers), we find that the transition between X-point acceleration and acceleration governed by island mergers should occur at a critical island width of $w/r_{0,\text{hot}} \sim 50$. Then, remembering that $w/L \sim 0.2$ for the largest islands (which will give the highest energy particles), we find that the transition width $w/r_{0,\text{hot}} \sim 50$ should correspond to a critical domain length of $L/r_{0,\text{hot}} \sim 250$, in agreement with the break in the curves of Fig. 11 (bottom panel).

---

[18] We have taken the reconnection rate in between the two merging islands to be of the order of $\sim 0.15\,c$ and we have considered that the magnetic field in the plasmoids is a factor of ~ 1.5 larger than the field B_0 in the inflow (see the fourth row in Fig. 5).
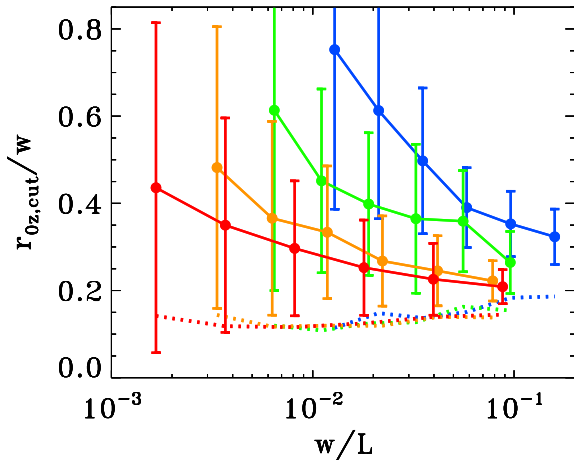
Figure 12. Positron anisotropy in the z-direction, as a function of the plasmoid size w and for different values of the system length, $L/r_{0,\mathrm{hot}} \simeq 127$ (blue), $L/r_{0,\mathrm{hot}} \simeq 257$ (green), $L/r_{0,\mathrm{hot}} \simeq 518$ (yellow) and $L/r_{0,\mathrm{hot}} \simeq 1130$ (red). In all the cases, the simulation timespan is $\sim 3.6\,L/c$. Each of the filled circles indicates the value of $r_{0i,\mathrm{cut}}/w$ with $i = +z$ (i.e. along the reconnection electric field), averaged among the plasmoids whose width falls in that range. Error bars indicate the standard deviation. In contrast, the dotted lines show the mean values of $r_{0i,\mathrm{cut}}/w$ with $i = -z$. For each choice of L, larger plasmoids are closer to isotropy. Also, small system lengths L, where the largest plasmoids are not much bigger than $r_{0,\mathrm{hot}}$, tend to overemphasize the degree of anisotropy.

For $L/r_{0,\mathrm{hot}} \gtrsim 300$, the ratio $r_{0,\mathrm{cut}}/L$ is expected to remain constant with L, since the energy of the highest energy particles accelerated in island mergers scales linearly with the width w of the largest plasmoids, which in turn is proportional to the system size L (see the top panel). Simulations in a small domain (Werner et al. 2016) are not able to reach this asymptotic limit, beyond the scaling $r_{0,\mathrm{cut}}^{\mathrm{max}}/L \propto L^{-1}$ that holds at small L.[19] Rather, we find that in the limit $L/r_{0,\mathrm{hot}} \gg 1$ of astrophysical interest, the highest energy particles accelerated by reconnection have a Larmor radius $r_{0,\mathrm{cut}} \sim 0.03L$, regardless of $L/r_{0,\mathrm{hot}}$ (here, we have implicitly assumed that the highest energy particles in the system are contained in magnetic islands, as we demonstrate in Appendix B). This can be regarded as the Hillas criterion (Hillas 1984) for relativistic reconnection.

We conclude this section by investigating the dependence of the z anisotropy of the particle distribution on the system length L. In Fig. 12, we quantify the z anisotropy by means of the Larmor radius of positrons at the upper cutoff of their z momentum spectrum, considering only positrons with $p_z > 0$ (solid lines with error bars) or $p_z < 0$ (dotted lines). The positron Larmor radius is plotted as a function of the island size w/L for different system lengths ($L/r_{0,\mathrm{hot}} \simeq 127$ in blue, $L/r_{0,\mathrm{hot}} \simeq 257$ in green, $L/r_{0,\mathrm{hot}} \simeq 518$ in yellow and $L/r_{0,\mathrm{hot}} \simeq 1130$ in red). For each value of $L/r_{0,\mathrm{hot}}$, the positron anisotropy decreases with increasing plasmoid width, as already discussed in Section 4.2. More interestingly, the degree of anisotropy at fixed w/L is significantly lower for larger system lengths $L/r_{0,\mathrm{hot}}$. Rather than being dependent on w/L, the level of z anisotropy seems to be a function of $w/r_{0,\mathrm{hot}}$, i.e. of the plasmoid width

normalized to plasma scales (rather than to the system length L). This is suggested in Fig. 12 by the fact that different solid curves appear to overlap, if we were to shift them along the horizontal axis by the corresponding value of $L/r_{0,\mathrm{hot}}$ (this, in fact, is equivalent to measuring w in units of $r_{0,\mathrm{hot}}$). This results from the fact that in small systems, the process of particle acceleration is dominated by the X-point stage, that occurs on plasma scales $\sim r_{0,\mathrm{hot}}$.

The pronounced anisotropy observed at small $L/r_{0,\mathrm{hot}}$ still bears memory of the anisotropy of particles accelerated at X-points (Cerutti et al. 2012, 2013; Kagan et al. 2016). In contrast, in large systems, most of the particles accelerated at X-points are efficiently isotropized in magnetic islands (SS14), resulting in a lower degree of anisotropy. It follows that the kinetic beaming effect described by Cerutti et al. (2012, 2013) and Kagan et al. (2016), due to the strong anisotropy of particles accelerated by reconnection, tends to be important only in small systems. Since realistic astrophysical systems typically have lengths $L/r_{0,\mathrm{hot}} \gg 1$, we conclude that the comoving particle distribution in the largest plasmoids, which are likely to give the brightest emission signatures, is nearly isotropic.

6 SUMMARY AND DISCUSSION

In this work, we have performed a suite of 2.5D PIC simulations of antiparallel relativistic reconnection in pair plasmas – 2D in space, but all three components of velocities and electromagnetic fields are tracked – to study the long-term evolution of the system, independently of the initial setup of the current sheet. We explore a range of flow magnetizations (from $\sigma = 3$ to 50), focusing on unprecedentedly large-scale systems with length $L \gg r_{0,\mathrm{hot}}$, where $r_{0,\mathrm{hot}} = \sqrt{\sigma}\,c/\omega_{\mathrm{p}}$ is the Larmor radius of particles heated/accelerated by reconnection. We find that a self-consistent by-product of the asymptotic physics is the continuous formation of a chain of plasmoids/magnetic islands, generated by the secondary tearing instability (Uzdensky et al. 2010). We argue that such plasmoids, quasi-spherical structures filled with high-energy particles and magnetic fields, can play a dominant role in the high-energy emission from relativistic astrophysical sources, such as PWNe and jets in AGNs and GRBs. We first summarize our findings on the reconnection physics and then briefly discuss their astrophysical implications.

6.1 Reconnection plasma physics summary

We have fully characterized the plasmoid properties as a function of their width w (transverse to the reconnection layer) and the flow magnetization σ, and our main conclusions can be summarized as follows:

(i) the plasmoids are nearly spherical, with length along the current sheet that is a factor of ~ 1.5 larger than the width. They are moderately denser than the inflowing plasma (a factor of a few, with only a moderate dependence on σ), with magnetic field strength averaged over the plasmoid volume that is ~ 50 per cent higher than the value B_0 in the inflow region. Both the magnetic and the kinetic energy density in the plasmoids scale linearly with the magnetization σ. The plasmoids are nearly in equipartition between particles and magnetic fields, with only a moderate dominance of the particle kinetic content, most pronounced in small plasmoids ($w/L \lesssim 0.02$).

(ii) Our choice of absorbing/outflow boundary conditions in the x-direction of the outflow – as opposed to the common choice of periodic boundaries – allows us to follow the system for many light crossing times, and to assess the statistical distributions of

---

[19] In the case of untriggered reconnection studied with periodic boundary conditions, the same requirement of $L/r_{0,\mathrm{hot}} \gtrsim 300$ should be imposed over the distance in between two neighbouring primary islands, resulting in a much more constraining condition on the overall box length (which typically includes many primary plasmoids).

plasmoid width w and magnetic flux Ψ. For large plasmoids ($\Psi/B_0L \gtrsim 0.01$), the differential distributions of w and Ψ both follow a -2 power-law distribution. Smaller plasmoids ($\Psi/B_0L \lesssim 0.01$) have harder distributions, with power-law slope around -1. The width distribution cuts off at $w/L \sim 0.2$ (and correspondingly, the flux distribution at $\Psi/B_0L \sim 0.2$). The results of our fully kinetic simulations are consistent with MHD simulations of non-relativistic (Huang & Bhattacharjee 2012; Loureiro et al. 2012) and relativistic (Takamoto 2013) reconnection.

(iii) We identify the particles belonging to each plasmoid, and we quantify their particle spectrum and anisotropy. We find that the Larmor radius $r_{0y,\text{cut}} = p_{y,\text{cut}}c/eB_0$ measured with the cut-off momentum $p_{y,\text{cut}}$ along the y-direction transverse to the current sheet scales almost linearly with the plasmoid width w, with the same constant of proportionality $r_{0y,\text{cut}}/w \sim 0.2$ at all magnetizations. This corresponds to the particles with the highest y momentum being barely confined in the plasmoids (i.e. a confinement criterion). The particle population is roughly isotropic in the x–y plane. In small islands, a strong degree of anisotropy in the positron distribution is observed along the $+z$-direction of the reconnection electric field (electrons have the opposite anisotropy), suggesting that direct acceleration at X-points plays an important role in the early stages of particle acceleration (Zenitani & Hoshino 2001; SS14; Nalewajko et al. 2015). In contrast, large islands are nearly isotropic, and the highest energy particles they contain are accelerated during island mergers (Guo et al. 2014, 2015; SS14). The transition between small anisotropic islands and large isotropic islands occurs at $w/r_{0,\text{hot}} \sim 50$, regardless of the overall system length L. It follows that, for a realistic astrophysical system with $L/r_{0,\text{hot}} \gg 1$, all but the smallest islands will be fairly isotropic. In contrast, in small computational domains, due to the lack of a sufficient separation of scales between the plasma scales and the system size, one might artificially overemphasize the degree of particle anisotropy (as in Cerutti et al. 2012, 2013; Kagan et al. 2016).

(iv) Small islands have a momentum distribution that is nearly thermal, since they cannot successfully confine the highest energy particles accelerated at X-points. In contrast, large islands have power-law momentum distributions, with a power-law slope $s \sim 3$ for $\sigma = 3$, $s \sim 2$ for $\sigma = 10$ and $s \sim 1.5$ for $\sigma = 50$. Such slopes are consistent with the values quoted in SS14, where the particle spectrum accounted for all the particles in the current sheet (and not just the particles trapped in plasmoids). This is expected, since we find that nearly all of the highest energy particles produced by reconnection are contained in the few largest plasmoids.

(v) By following the trajectory of individual plasmoids over time, we find that the life of secondary plasmoids from birth to adulthood is characterized by two phases: first they grow, then they go. They are born on microscopic plasma scales, and they grow by accretion, with a constant comoving growth rate $\beta_{\text{g}} = \text{d}w/c\,\text{d}t \sim 0.1$ that has only a weak dependence on magnetization. For all the values of σ we explore, we find that β_{g} is about half of the reconnection inflow rate $|v_{\text{in}}|/c$, which slightly increases from $|v_{\text{in}}|/c \simeq 0.1$ for $\sigma = 3$ up to $|v_{\text{in}}|/c \simeq 0.2$ for $\sigma = 50$. The weak dependence of $|v_{\text{in}}|/c$ on magnetization is consistent with the predictions of Lyubarsky (2005)'s model of relativistic reconnection.

(vi) Occasionally, a plasmoid in the reconnection layer can reach a 'monster' width of $w \sim 0.2\,L$, consistent with the results of MHD simulations of non-relativistic reconnection (Loureiro et al. 2012). The size of the monster plasmoid is always a fixed fraction of the system length L, for different choices of $L/r_{0,\text{hot}}$, and their typical recurrence time is $\sim 2.5\,L/c$. Monster plasmoids have

nearly isotropic particle distributions and they contain the highest energy particles in the system. For sufficiently large domains ($L/r_{0,\text{hot}} \gtrsim 300$), we show that the Larmor radius of the highest energy particles is $r_{0,\text{cut}}^{\text{max}} \sim 0.03\,L$, i.e. a constant fraction of the system size. This can be regarded as the Hillas criterion (Hillas 1984) for relativistic reconnection. In contrast, simulations in a small domain with $L/r_{0,\text{hot}} \lesssim 300$ (Werner et al. 2016) would not be able to reach this asymptotic limit, beyond the scaling $r_{0,\text{cut}}^{\text{max}}/L \propto L^{-1}$ that we observe at small L, which is expected from the fact that early particle acceleration at X-points yields a maximum Larmor radius $r_{0,\text{cut}}^{\text{max}} \sim 10\,r_{0,\text{hot}}$ regardless of L.

(vii) After their growth, the plasmoids are accelerated towards the boundaries of the domain by the tension force of the magnetic field lines. We find that the bulk four-velocity of the accelerating plasmoids follows a universal profile $\Gamma v_{\text{out}}/c \simeq \sqrt{\sigma}\tanh[\beta_{\text{acc}}(x - x_0)/\sqrt{\sigma}w]$, where the acceleration rate $\beta_{\text{acc}} \simeq 0.12$ is nearly insensitive to the flow magnetization. Here, x_0 is the plasmoid location at birth. This implies that at large distances ($\beta_{\text{acc}}|x - x_0| \gtrsim \sqrt{\sigma}w$), the plasmoid four-velocity approaches $\sim\sqrt{\sigma}\,c$, i.e. the plasmoid moves at nearly the Alfvén speed $v_{\text{A}} = \sqrt{\sigma/(\sigma+1)}\,c$. This is indeed the outflow speed from relativistic reconnection predicted by Lyubarsky (2005), as we have verified for all the magnetizations we explore (earlier studies in smaller domains could not capture this asymptotic limit, see Cerutti et al. 2013; Guo et al. 2015; Kagan et al. 2016). On the other hand, at small distances ($\beta_{\text{acc}}|x - x_0| \lesssim \sqrt{\sigma}w$), the scaling is $\Gamma v_{\text{out}}/c \sim \beta_{\text{acc}}(x - x_0)/w$. It follows that (i) monster plasmoids with $w/L \sim 0.2$ leave the system at trans-relativistic speeds; (ii) the largest plasmoids capable of reaching the end of the current sheet with the terminal four-velocity $\sim\sqrt{\sigma}\,c$ will have a final width of $w/L \sim \beta_{\text{acc}}/\sqrt{\sigma}$, i.e. they are systematically smaller at higher magnetizations.

We conclude with a few caveats. In this work, we have only focused on electron–positron reconnection, but we claim that all of our results will hold for electron–proton reconnection, since in the relativistic regime $\sigma \gg 1$, the field dissipation results in nearly equal amounts of energy transferred to protons as to electrons, as we have demonstrated in SPG15. So, the mean energy per particle of the two species is nearly the same, as it is the case for an electron–positron plasma. From a numerical point of view, electron–ion reconnection is much more demanding than electron–positron reconnection, since the system needs to have a length (in cells) larger by $\sqrt{m_i/m_\text{e}}$ in each direction (here m_i and m_e are the proton and electron masses), and the evolution needs to be followed for a factor $\sqrt{m_i/m_\text{e}}$ longer. So, it will be even more challenging to reach the asymptotic state described in this work, where the largest islands are nearly isotropic, the outflow speed reaches the expected terminal velocity, and the maximum energy of accelerated particles increases linearly with the system size. Studies in small systems will tend to artificially overemphasize the importance of effects that are only appropriate at microscopic plasma scales, and irrelevant for $L/r_{0,\text{hot}} \gg 1$ systems of astrophysical interest.

Also, we have only explored the case of anti-parallel fields, i.e. without a guide field perpendicular to the alternating fields. For stronger guide fields, one expects that the efficiency of reconnection will be reduced and the plasmoids will become more magnetically dominated, as we have shown in SPG15. A complete investigation of the plasmoid properties in guide-field reconnection will be presented elsewhere. Finally, our simulations are two-dimensional. As shown in SS14, the long-term evolution of 3D antiparallel reconnection is remarkably similar to the 2D physics, both in terms of the dynamics of the reconnection layer and the efficiency of particle

acceleration. Still, the structure of plasmoids/flux ropes in 3D remains to be investigated.

6.2 Astrophysical implications

A large recent volume of research in the field has revealed that relativistic reconnection is a highly dynamical process that involves a broad range of physical processes on very different time-scales; all of which can have direct observational signatures. Consider a reconnection layer of length L where magnetic energy is dissipated in a magnetized fluid of total volume $\sim L^3$ (for simplicity, we take all the scales of the problem to be comparable). Reconnection proceeds on a global time-scale $t_{rec} \sim L/|v_{in}| \sim 10\,L/c$ until it exhausts all the available energy in the system. The dissipated energy ends up in ultra-relativistic particles that are mostly contained in plasmoids. The emission from the layer, therefore, comes in bursts or flares whose duration is closely related to the time it takes for the plasmoids to grow and leave the layer. The largest plasmoids take a time $\sim L/c$ to form, and they leave the reconnection layer at mildly relativistic speeds ($\Gamma|v_{out}|/c \sim 1$). Powerful flares are therefore expected from these plasmoids on a time-scale $t_l \lesssim L/c$. Smaller plasmoids are accelerated to relativistic speeds $\Gamma \sim \sqrt{\sigma}$ and they radiate anisotropically, as a result of their bulk motion. When the observer lies along the current sheet, small plasmoids are viewed as very powerful and extremely fast evolving $t_s \ll L/c$ emitters.

The detailed shape and variety of flares expected from a current sheet and their implications for blazar jets are presented elsewhere (Petropoulou et al. 2016). Here, we estimate the maximum energies that particles can achieve in reconnection layers in blazar jets and during flares from the Crab nebula. Let us assume a flow with a bulk motion Γ_b that beams its emission towards the observer with corresponding Doppler factor $\delta \sim \Gamma_b$. Consider a major flare from this flow powered by a large plasmoid. The observed duration of the flare is $t_f \sim L/c\delta$, which constrains the size of the reconnection layer. From our 'Hillas criterion for reconnection,' that dictates the maximum particle energy associated with this plasmoid, we find that the gyro-radius of the highest energy particles is $r_g \sim 0.03\,L$. The energy of the cosmic ray particles is $E_{CR} = \Gamma_b eBr_g \sim 0.03\Gamma_b \delta eBct_f$, were the magnetic field B is measured in the rest frame of the flow.

Blazar jets show major flares on a time-scale of hours/days (as a reference value, we set $t_f = 10^5 t_5$ s). The 'blazar zone' is characterized by typical $\Gamma_b \sim \delta \gtrsim 10$, while the magnetic field strength is $B \sim 1G$ (e.g. Celotti & Ghisellini 2008).[20] Protons present in the reconnecting plasma can be accelerated to $E_{CR} \sim 3 \times 10^{18}\Gamma_1\delta_1 B_0 t_5$ eV. Here, $\Gamma_1 = \Gamma_b/10$, $\delta_1 = \delta/10$ and $B_0 = B/1\,G$. Therefore, protons can possibly reach the highest observed energies of $E \sim 10^{20}$ eV for sufficiently fast jet flows $\Gamma_b \gtrsim 10$ with field strengths $B \gtrsim 1G$.

The *Fermi* and AGILE satellites have detected a number of $\sim$day-long flares at GeV energies from the Crab nebula, which surprisingly falsify the widely believed standard candle nature of the high-energy Crab emission. During these events, the Crab nebula γ-ray flux above 100 MeV exceeded its average value by a factor of several or higher (Abdo 2011; Buehler et al. 2012). *Fermi* acceleration at the termination shock of the Crab nebula fails to explain the observed GeV flares. In contrast, rapid conversion of magnetic field energy into particle energy via magnetic reconnection has been recently proposed to explain the Crab flares (e.g. Cerutti et al. 2013, 2014).

---

[20] This value of magnetic field is typical only for leptonic models. In hadronic models $B \sim 100\,G$.

For magnetic field strengths in the nebula of $B \sim$ several mG, $t_f = 10^5 t_5$ s and allowing for a modest relativistic motion of the emitting plasmoid $\Gamma_b \simeq \delta \simeq 2$, we find that pairs can be accelerated up to $E_{CR} \sim 1$PeV. This energy is sufficient to potentially explain the extreme synchrotron peak during the Crab flares. Radiative cooling has, however, to be taken into account self-consistently when one considers the maximum attainable particle energy. This is left for future work.

REFERENCES

Abdo A. A. et al., 2011, Science, 331, 739
Bai X.-N., Caprioli D., Sironi L., Spitkovsky A., 2015, ApJ, 809, 55
Begelman M. C., 1998, ApJ, 493, 291
Belyaev M. A., 2015, New Astron., 36, 37
Bessho N., Bhattacharjee A., 2005, Phys. Rev. Lett., 95, 245001
Bessho N., Bhattacharjee A., 2007, Phys. Plasmas, 14, 056503
Bessho N., Bhattacharjee A., 2010, Phys. Plasmas, 17, 102104
Bessho N., Bhattacharjee A., 2012, ApJ, 750, 129
Buehler R. et al., 2012, ApJ, 749, 26
Buneman O., 1993, Computer Space Plasma Physics. Terra Scientific, Tokyo, p. 67
Celotti A., Ghisellini G., 2008, MNRAS, 385, 283
Cerutti B., Werner G. R., Uzdensky D. A., Begelman M. C., 2012, ApJ, 754, L33
Cerutti B., Werner G. R., Uzdensky D. A., Begelman M. C., 2013, ApJ, 770, 147
Cerutti B., Werner G. R., Uzdensky D. A., Begelman M. C., 2014, ApJ, 782, 104
Cerutti B., Philippov A., Parfrey K., Spitkovsky A., 2015, MNRAS, 448, 606
Daughton W., Karimabadi H., 2007, Phys. Plasmas, 14, 072303
Daughton W., Scudder J., Karimabadi H., 2006, Phys. Plasmas, 13, 072101
Drake J. F., Swisdak M., Che H., Shay M. A., 2006, Nature, 443, 553
Drenkhahn G., Spruit H. C., 2002, A&A, 391, 1141
Fermo R. L., Drake J. F., Swisdak M., 2010, Phys. Plasmas, 17, 010702
Giannios D., 2008, A&A, 480, 305
Giannios D., 2013, MNRAS, 431, 355
Giannios D., Uzdensky D. A., Begelman M. C., 2009, MNRAS, 395, L29
Giannios D., Uzdensky D. A., Begelman M. C., 2010, MNRAS, 402, 1649
Guo F., Li H., Daughton W., Liu Y.-H., 2014, Phys. Rev. Lett., 113, 155005
Guo F., Liu Y.-H., Daughton W., Li H., 2015, ApJ, 806, 167
Guo F. et al., 2016, ApJ, 818, L9
Hesse M., Zenitani S., 2007, Phys. Plasmas, 14, 112102
Hillas A. M., 1984, ARA&A, 22, 425
Huang Y.-M., Bhattacharjee A., 2012, Phys. Rev. Lett., 109, 265002
Jaroschek C. H., Lesch H., Treumann R. A., 2004, ApJ, 605, L9
Kagan D., Milosavljević M., Spitkovsky A., 2013, ApJ, 774, 41
Kagan D., Sironi L., Cerutti B., Giannios D., 2015, Space Sci. Rev., 191, 545
Kagan D., Nakar E., Piran T., 2016, preprint (arXiv:1601.07349)

Kirk J. G., Skjæraasen O., 2003, ApJ, 591, 366
Liu W., Li H., Yin L., Albright B. J., Bowers K. J., Liang E. P., 2011, Phys. Plasmas, 18, 052105
Liu Y.-H., Guo F., Daughton W., Li H., Hesse M., 2015, Phys. Rev. Lett., 114, 095002
Loureiro N. F., Samtaney R., Schekochihin A. A., Uzdensky D. A., 2012, Phys. Plasmas, 19, 042303
Lyubarsky Y. E., 2003, MNRAS, 345, 153
Lyubarsky Y. E., 2005, MNRAS, 358, 113
Lyubarsky Y., Kirk J. G., 2001, ApJ, 547, 437
Lyubarsky Y., Liverts M., 2008, ApJ, 682, 1436
Lyutikov M., Blandford R., 2003, preprint (arXiv:astro-ph/0312347)
Lyutikov M., Uzdensky D., 2003, ApJ, 589, 893
Lyutikov M., Sironi L., Komissarov S., Porth O., 2016, preprint (arXiv:1603.05731)
Melzani M., Walder R., Folini D., Winisdoerffer C., Favre J. M., 2014, A&A, 570, A112
Murphy N. A., Young A. K., Shen C., Lin J., Ni L., 2013, Phys. Plasmas, 20, 061211
Nalewajko K., Uzdensky D. A., Cerutti B., Werner G. R., Begelman M. C., 2015, ApJ, 815, 101
Pétri J., Lyubarsky Y., 2007, A&A, 473, 683
Petropoulou M., Giannios D., Sironi L., 2016, preprint (arXiv:1606.07447)
Romanova M. M., Lovelace R. V. E., 1992, A&A, 262, 26
Sironi L., Spitkovsky A., 2009, ApJ, 698, 1523
Sironi L., Spitkovsky A., 2011a, ApJ, 726, 75
Sironi L., Spitkovsky A., 2011b, ApJ, 741, 39
Sironi L., Spitkovsky A., 2012, Comput. Sci. Discovery, 5, 014014
Sironi L., Spitkovsky A., 2014, ApJ, 783, L21 (SS14)
Sironi L., Spitkovsky A., Arons J., 2013, ApJ, 771, 54
Sironi L., Petropoulou M., Giannios D., 2015, MNRAS, 450, 183 (SPG15)
Spitkovsky A., 2005, in Bulik T., Rudak B., Madejski G., eds, AIP Conf. Proc. Vol. 801, Astrophysical Sources of High Energy Particles and Radiation. Am. Inst. Phys., New York, p. 345
Spruit H. C., 2010, in Belloni T., ed., Lecture Notes in Physics, Vol. 794, Theory of Magnetically Powered Jets. Springer-Verlag, Berlin, p. 233
Spruit H. C., Daigne F., Drenkhahn G., 2001, A&A, 369, 694
Synge J. L., 1957, The Relativistic Gas. North-Holland, Amsterdam, p. 33
Takamoto M., 2013, ApJ, 775, 50
Thompson C., 1994, MNRAS, 270, 480
Thompson C., 2006, ApJ, 651, 333
Usov V. V., 1994, MNRAS, 267, 1035
Uzdensky D. A., Loureiro N. F., Schekochihin A. A., 2010, Phys. Rev. Lett., 105, 235002
Werner G. R., Uzdensky D. A., Cerutti B., Nalewajko K., Begelman M. C., 2016, ApJ, 816, L8
Yin L., Daughton W., Karimabadi H., Albright B. J., Bowers K. J., Margulies J., 2008, Phys. Rev. Lett., 101, 125001
Zenitani S., Hoshino M., 2001, ApJ, 562, L63
Zenitani S., Hoshino M., 2005, Phys. Rev. Lett., 95, 095001
Zenitani S., Hoshino M., 2007, ApJ, 670, 702
Zenitani S., Hoshino M., 2008, ApJ, 677, 530

SUPPORTING INFORMATION

APPENDIX A: PLASMOID SPATIAL PROFILES

Fig. A1 presents the spatial profiles of various comoving quantities along the y-direction transverse to the current sheet, for the three values of magnetization that we explore in this work ($\sigma = 3$ on the left, $\sigma = 10$ in the middle and $\sigma = 50$ on the right). In each panel, curves of different colours correspond to a different bin of plasmoid width w (from blue to red in order of increasing w/L), and each line is obtained by averaging the y-profile at the plasmoid x-location over all the plasmoids whose width falls in that range. The corresponding plasmoid width can be read from the separation, along the y-direction, between the two filled circles, that denote the plasmoid boundaries along y.

In the top row, we show the y-profiles of the plasmoid comoving density, in units of the particle number density n_0 far from the current sheet. By plotting on a log–log scale (not shown), we can measure that the density scales with distance from the current sheet roughly as $n \propto (|y|/w)^{-1.0}$, with only a slight tendency for steeper profiles at higher magnetizations. This scaling implies that the plasmoid mass is mostly sensitive to the value of the density at the plasmoid outskirts. The top row in Fig. A1 shows that the density in the outskirts is a weak function of the magnetization, which explains why the scaling $\propto \sqrt{\sigma}$ expected for the mean density in relativistic reconnection (Lyubarsky 2005) is not realized in the second row of Fig. 5.[21] As we have argued in Section 4.1, the scaling $n \propto \sqrt{\sigma}$ is to be expected only for the fastest plasmoids, that can reach the terminal four-velocity $\sim \sqrt{\sigma}\, c$. As described in Section 4.4, only few plasmoids approach $\sim \sqrt{\sigma}\, c$ for $\sigma = 50$, which justifies why the density in the plasmoid outskirts in the top row of Fig. A1 does not appreciably increase between $\sigma = 10$ and 50.

The second row in Fig. A1 illustrates the y-profile of the co-moving magnetic energy fraction. Since the slice along y where we compute the profiles goes through the plasmoid centre, the magnetic field B is dominated by its x-component, which is Lorentz invariant. For this reason, we can extend the profiles in the second row of Fig. A1 outside of the plasmoid contour (see the dotted lines), without ambiguity (i.e. the profiles of plasmoids with different speeds can be meaningfully averaged). By plotting on a log–log scale (not shown), we can measure that the magnetic energy scales as $\epsilon_{\rm B} \propto (|y|/w)^{-1.2}$, regardless of the magnetization. This scaling implies that most of the magnetic energy is contributed by the plasmoid outskirts (filled circles in the plot). Since Fig. A1 shows that the magnetic energy at the plasmoid boundary scales as $\propto \sigma$ (e.g. see the red curves, for the largest islands), the same scaling is expected for the volume-averaged magnetic energy fraction, as indeed found in the fourth row of Fig. 5.

For a given magnetization, Fig. A1 reveals that the magnetic field at the plasmoid boundary has a strong dependence on the island width, with smaller islands systematically residing in regions with weaker fields. As described in Section 3, this trend is due to field lines wrapping around a large island, so that the smaller islands in its vicinity will preferentially lie in a region where the field lines are less densely spaced, and so the field is weaker. The fact that smaller islands are more likely to reside in 'wells' of magnetic energy, as revealed by the second row of Fig. A1, explains the apparent lack of

[21] Yet, such a scaling seems to be fulfilled by the peak density (i.e. at $y \sim 0$) of the largest islands (compare the three red curves for different values of σ in the top row of Fig. A1).
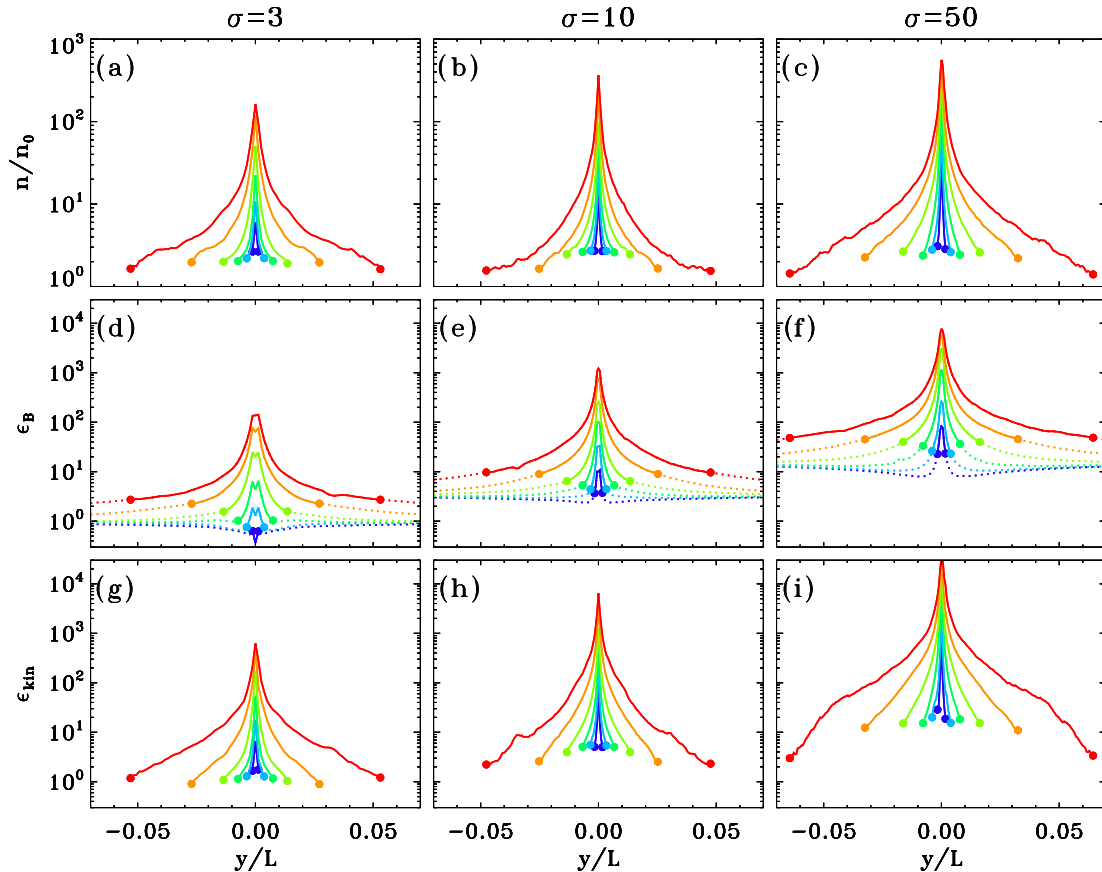
Figure A1. 1D profiles of various plasmoid properties, along the direction y perpendicular to the current layer, for three values of the magnetization, as indicated at the top ($\sigma = 3$ in the left-hand column, $\sigma = 10$ in the middle column, and $\sigma = 50$ in the right-hand column). In each panel, curves of different colours correspond to a different bin of plasmoid width w (from blue to red in order of increasing w), and each line is obtained by averaging the y-profile at the plasmoid x-location over all the plasmoids whose width falls in that range. The corresponding plasmoid width can be read from the separation, along the y-direction, between the two filled circles, that denote the plasmoid boundaries along y. The bins in width are the same as in Fig. 7. From the top to the bottom row, we plot: (a)–(c) the comoving density n, in units of the density n_0 far from the current sheet; (d)–(f) the magnetic energy fraction $\epsilon_B = B^2/8\pi n_0 mc^2$, where B is measured in the plasmoid comoving frame; (g)–(i) the internal energy fraction $\epsilon_{kin} = (\langle\gamma\rangle - 1) n/n_0$, where $\langle\gamma\rangle$ is the mean particle Lorentz factor in the plasmoid frame. In the second row of panels, we plot the profile of ϵ_B outside the plasmoids with dotted lines. Here, $B \sim |B_x|$, which is Lorentz invariant, so the ϵ_B profile outside the plasmoids does not depend on the plasmoid velocity, and the profiles of plasmoids with different speeds can be meaningfully averaged. This argument does not hold for n or ϵ_{kin}.

magnetic flux and magnetic energy seen in Fig. 5 (third and fourth row) at small plasmoid widths.

The bottom row of panels in Fig. A1 describes the profiles of the comoving particle kinetic energy. On a log–log scale (not shown), we find that the kinetic energy fraction scales with distance from the sheet as $\epsilon_{kin} \propto (|y|/w)^{-1.4}$, regardless of the magnetization. By comparing with the density profile, we find that the mean kinetic energy per particle scales with distance as $\propto (|y|/w)^{-0.4}$, with only a slight tendency for a harder slope at higher σ. This scaling for the mean energy per particle (i.e. for the temperature) is consistent with adiabatic heating, since for an ultra-relativistic gas, it should depend on the density as $\propto n^{1/3} \propto (|y|/w)^{-0.3}$. The scaling $\epsilon_{kin} \propto (|y|/w)^{-1.4}$ of the kinetic energy fraction is slightly steeper than the magnetic energy profile, so that the island core will typically be dominated by the particle kinetic energy, whereas the magnetic energy will govern the plasmoid outskirts.

As in the case of the magnetic energy fraction, the scaling $\epsilon_{kin} \propto (|y|/w)^{-1.4}$ implies that most of the kinetic energy is contributed by the plasmoid outskirts. There, ϵ_{kin} scales as $\propto \sigma$ (e.g. see the red curves, for the largest islands), so the same scaling is expected for the volume-averaged kinetic energy fraction, as indeed found in the

fifth row of Fig. 5. Unlike the magnetic energy fraction, the value of the kinetic energy at the plasmoid boundary does not appreciably depend on the plasmoid size, at fixed σ (see the filled circles in the bottom row). In turn, this explains why the kinetic energy fraction in the fifth row of Fig. 5 is nearly constant with respect to the plasmoid width (especially as compared to the magnetic energy fraction in the fourth row of Fig. 5, which shows a significant deficit at small sizes).

APPENDIX B: COMPARISON OF THE SPECTRUM IN PLASMOIDS WITH THE OVERALL SPECTRUM

Fig. B1 illustrates how the positron spectrum in the plasmoids compares with the positron spectrum in the overall current sheet (i.e. including also the region in between plasmoids). The spectra are measured in the laboratory frame for the three values of magnetization that we explore in this work ($\sigma = 3$ in the left-hand column, $\sigma = 10$ in the middle column, and $\sigma = 50$ in the right-hand column). In each panel, we plot the overall spectrum from the current sheet (blue lines; integrated over the whole reconnection layer and
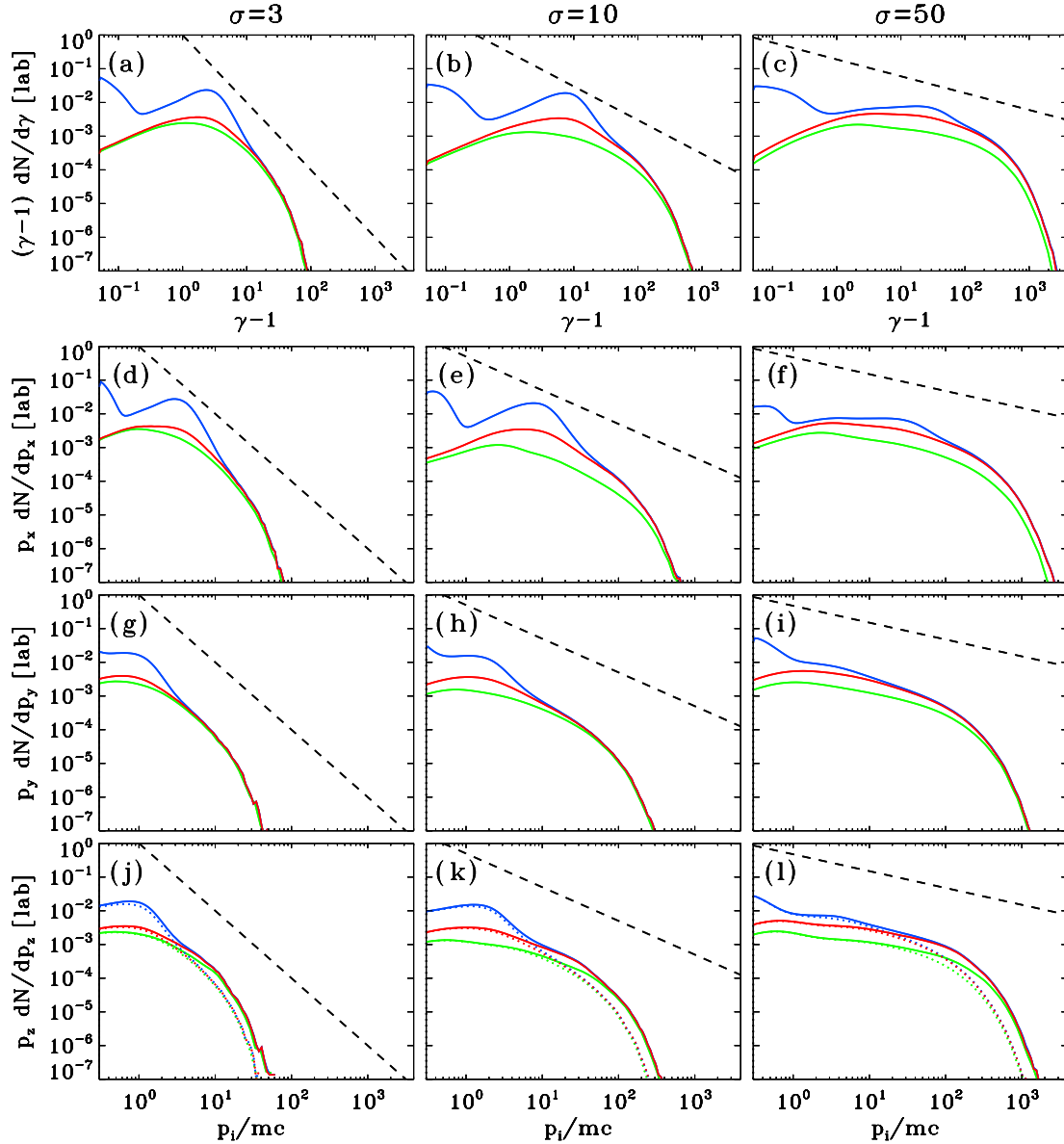
Figure B1. Positron energy and momentum spectra in the laboratory frame, for three values of the magnetization, as indicated at the top ($\sigma = 3$ in the left-hand column, $\sigma = 10$ in the middle column, and $\sigma = 50$ in the right-hand column). In each panel, we plot the overall spectrum from the current sheet (blue lines; integrated over the whole reconnection layer and over the timespan of our simulations), the spectrum of plasmoids (red lines; integrated over all the plasmoids at all times), and the cumulative spectrum from the five largest plasmoids (green lines; integrated over the history of the five largest plasmoids). We plot: (a)–(c) the positron energy spectrum in the laboratory frame; (d)–(f) the positron p_x spectrum in the laboratory frame; (g)–(i) the positron p_y spectrum in the laboratory frame; (j)–(l) the positron p_z spectrum in the laboratory frame, differentiating between positrons with $p_z > 0$ (solid curves) and $p_z < 0$ (dotted curves). For reference, we plot with black dashed lines a power law with slope $s = 3$ for $\sigma = 3$, $s = 2$ for $\sigma = 10$ and $s = 1.5$ for $\sigma = 50$. The plot shows that the highest energy particles are contained within the largest plasmoids.

over the timespan of our simulations), the spectrum of plasmoids (red lines; integrated over all the plasmoids at all times), and the cumulative spectrum from the five largest plasmoids (green lines; integrated over the history of the five largest plasmoids).

Both the energy spectra in the top row and the momentum spectra in the other panels suggest that the highest energy particles always belong to a plasmoid. In all the panels, the blue and red curves overlap at the high-energy end. Even more dramatically, most of the high-energy particles are contained in the few largest plasmoids (compare with the green curves, which only account for the five largest plasmoids). It follows that the maximum energy of particles accelerated in reconnection is identical to the maximum energy of

particles contained in plasmoids, which validates the generality of the Hillas criterion discussed in Section 5.

Fig. B1 confirms what we had anticipated in Section 4.2, i.e. the spectral slope of the largest plasmoids (green curves) asymptotes to $s \sim 3$ for $\sigma = 3$, $s \sim 2$ for $\sigma = 10$ and $s \sim 1.5$ for $\sigma = 50$, as indicated by the dashed black lines. Such slopes are consistent with the values quoted in SS14, where the particle spectrum was integrated over the whole current sheet. As Fig. B1 suggests, this is because the spectrum integrated over the whole layer is actually dominated by the few largest islands. It is then quite natural to expect that the spectral slope of the largest islands in Fig. B1 is comparable to the power-law index found in SS14.

In the particle energy spectra of the top row, the excess of particles at intermediate energies in the blue line (as compared to the red line) is due to hot particles in the reconnection outflow that do not belong to plasmoids. They move with a bulk Lorentz factor $\propto \sqrt{\sigma}$ and their mean temperature also scales as $\propto \sqrt{\sigma}$. Overall, this implies that their mean energy in the lab frame should scale as $\propto \sigma$, as indeed observed in the top row of Fig. B1 (see the peak at $\gamma - 1$ ~ 3 for $\sigma = 3$, at $\gamma - 1 \sim 7$ for $\sigma = 10$ and at $\gamma - 1 \sim 30$ for $\sigma = 50$). A signature of this bump at intermediate energies is also seen in the spectrum of small plasmoids (compare the red curve in panel b with the green line, showing that such bump is absent in the spectrum of the largest plasmoids). In simulations with periodic boundaries, where the spectrum at any given time is dominated by the particle content in the largest primary islands, one would expect that such bump at intermediate energies would be buried underneath the broad non-thermal spectrum of the largest islands, as it was indeed the case in SS14.

Since the particles that populate the bump at intermediate energies are preferentially moving along the *x*-direction of the outflow, a similar signature should appear in the second row of Fig. B1, as it is indeed observed. In the *y* and *z* momentum spectra, i.e. in the directions perpendicular to the bulk outflow, one should still see the thermal component of this particle population, whose temperature scales as $\propto \sqrt{\sigma}$. In fact, this explains the bump appearing in the third and bottom rows at trans-relativistic momenta, with a clear tendency for the peak momentum to increase with magnetization (the peak is located at $\sim 0.8\,mc$ for $\sigma = 3$, at $\sim 1.5\,mc$ for $\sigma = 10$ and at $\sim 3\,mc$ for $\sigma = 50$).

In the bottom row, we present the positron p_z spectrum in the laboratory frame, differentiating between positrons with $p_z > 0$ (solid curves) and $p_z < 0$ (dotted curves). This shows that the momentum spectrum in the $+z$-direction of the reconnection electric field is slightly harder than along the $-z$-direction (or along the *y*-direction). The asymmetry between the $p_z > 0$ and $p_z < 0$ momentum spectra is most pronounced at the highest energies, in agreement with the argument in Section 4.2, i.e. the anisotropy in large islands is driven by the curvature and ∇B drift speed, which, for a fixed island width, is an increasing function of the particle energy.

This paper has been typeset from a TEX/LATEX file prepared by the author.